energies

MDPI

Review

Towards Integration of Two-Dimensional Hexagonal Boron Nitride (2D h-BN) in Energy Conversion and Storage Devices

Shayan Angizi [1,†], Sayed Ali Ahmad Alem [2,†] and Amir Pakdel [3,*]

[1] Department of Chemistry and Chemical Biology, McMaster University, 1280 Main St. W., Hamilton, ON L8S 4M1, Canada; angizis@mcmaster.ca
[2] Department of Chemistry, Materials and Chemical Engineering, Politecnico di Milano, Piazza Leonardo da Vinci 32, 20133 Milan, Italy; sayedali.alem@mail.polimi.it
[3] Department of Mechanical, Manufacturing & Biomedical Engineering, Trinity College Dublin, The University of Dublin, D02 PN40 Dublin, Ireland
* Correspondence: pakdela@tcd.ie
† These authors contributed equally to this work.

Abstract: The prominence of two-dimensional hexagonal boron nitride (2D h-BN) nanomaterials in the energy industry has recently grown rapidly due to their broad applications in newly developed energy systems. This was necessitated as a response to the demand for mechanically and chemically stable platforms with superior thermal conductivity for incorporation in next-generation energy devices. Conventionally, the electrical insulation and surface inertness of 2D h-BN limited their large integration in the energy industry. However, progress on surface modification, doping, tailoring the edge chemistry, and hybridization with other nanomaterials paved the way to go beyond those conventional characteristics. The current application range, from various energy conversion methods (e.g., thermoelectrics) to energy storage (e.g., batteries), demonstrates the versatility of 2D h-BN nanomaterials for the future energy industry. In this review, the most recent research breakthroughs on 2D h-BN nanomaterials used in energy-based applications are discussed, and future opportunities and challenges are assessed.

Keywords: two-dimensional hexagonal boron nitride; battery; supercapacitor; thermoelectricity; fuel cell; solar cell

Citation: Angizi, S.; Alem, S.A.A.; Pakdel, A. Towards Integration of Two-Dimensional Hexagonal Boron Nitride (2D h-BN) in Energy Conversion and Storage Devices. *Energies* **2022**, *15*, 1162. https://doi.org/10.3390/en15031162

Academic Editor: Trung Van Nguyen

Received: 12 December 2021
Accepted: 1 February 2022
Published: 4 February 2022

1. Introduction

The ever-growing importance of green energy production/storage units to reduce the carbon footprint of fossil fuels has motivated researchers to explore new materials to enhance the efficiency of conventional energy technologies [1,2]. Two-dimensional (2D) materials derived from layered structures have shown to be promising candidates for the future generation of energy devices. Their properties such as ultra-high specific surface area, low absorption energy, high thermochemical stability, and biocompatibility have opened a window for highly efficient energy conversion/storage units [3]. Pioneering 2D materials in this regard include graphene, graphene oxide and transition metal dichalcogenides (TMDs). Other recently emerged 2D morphologies such as transition metal carbides, nitrides or carbonitrides (MXene) [4], boron carbon nitride ($B_xC_yN_z$) [5] and borophene [6] have also been of great interest due to their tunable surface chemistry and stoichiometric-dependent physical/chemical characteristics.

2D hexagonal boron nitride (h-BN) has also recently become a highly demanded energy materials functioning in many applications, from electrodes and electrolytes in batteries to membranes or catalysts in fuel cell units [7,8]. A recent wave of research on 2D h-BN-based energy applications, shown in Figure 1a,b, originates from the synergistic impacts of high thermal and chemical stabilities, superior thermal conductivity, and the electrically insulative nature of 2D h-BN [8–10]. The term h-BN refers to a layered nanomorphology of

boron (B) and nitrogen (N) atoms in a sp^2 hybridized honeycomb-shaped lattice [11,12]. The van der Waals interactions maintain the vertical stacking of the layers, resembling a graphitic structure [13], while the in-plane B-N bonds are covalent (σ) with partial ionicity due to electronegativity difference between the B and N (Figure 1c) [14]. The B-N bond strength offers excellent mechanical robustness, but on the other hand, the lack of pi (π) electrons on each plane minimizes the surface interactions caused by π-π forces [15]. Therefore, h-BN shows superior chemical stability when compared to other layered materials such as graphite or transition metal dichalcogenides (TMDs), where π-π conjugations dominate the surface interaction mechanisms [16]. Nevertheless, the partially charged sites on the surface (B positive, N negative) can be anchoring sites for Lewis acid-base interactions [17,18]. In fact, the existing empty orbital in B and a lone pair in N offers a promising pathway for selective functionalization of 2D h-BN nanomaterials [19]. The functionalization of 2D h-BN allows the modulation of surface chemistry to acquire the desired properties while the intrinsic characteristics are preserved [20,21]. For instance, hydroxylation of 2D h-BN enhances its water dispersibility, fluorination intensifies its photoluminescent emission, edge amination enhances its surface acid-base interactions, and point defects amplify its catalytic activities. These examples reveal that surface modification is the key to harnessing the full capability of 2D h-BN nanomaterials [22,23].

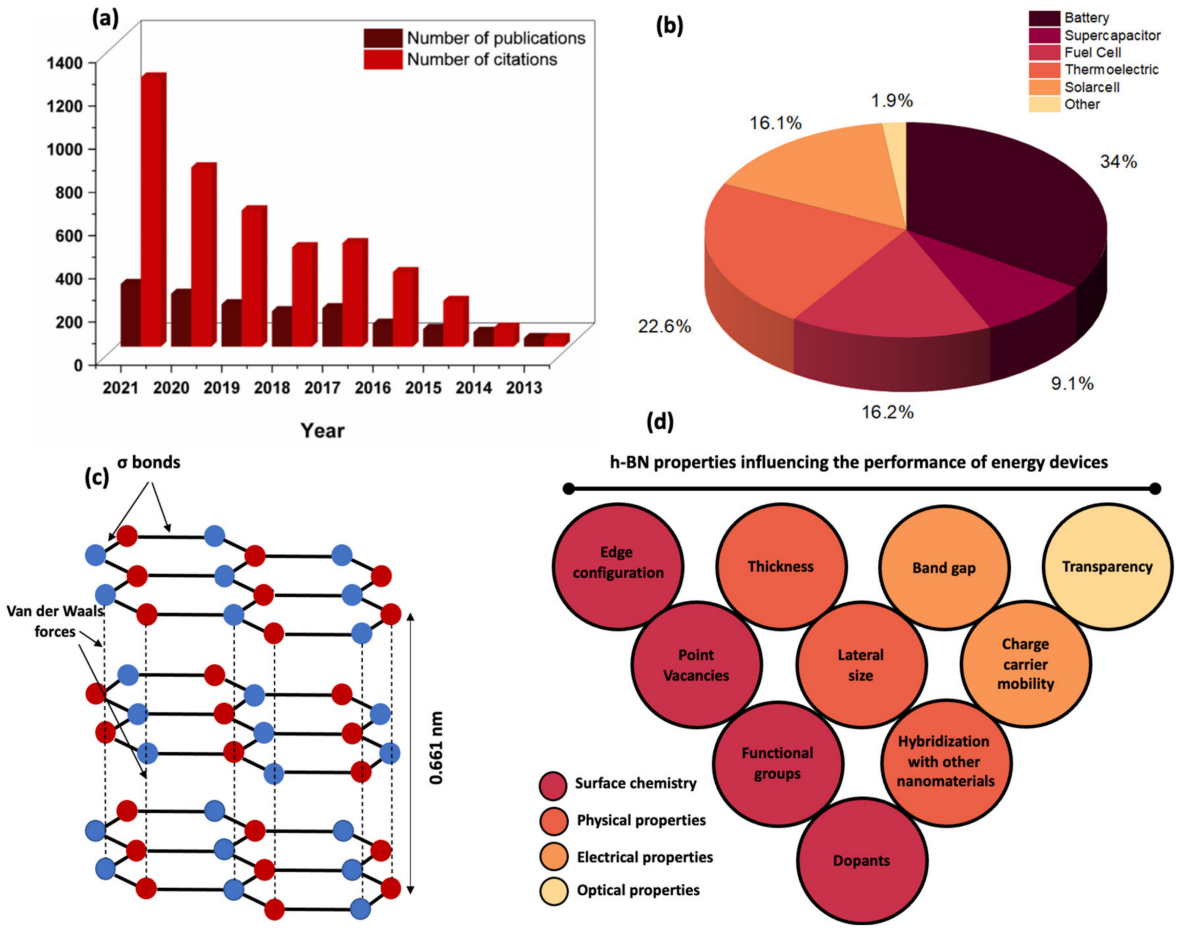

Figure 1. (**a**) The number of publications and citations on energy applications of h-BN per year based on the Scopus database. (**b**) The publication distribution pie chart of h-BN applications in energy research. (**c**) Schematic illustration of bulk h-BN crystal structure: in-plane σ bonds and cross-plane van der Waals interactions. (**d**) Diagram of h-BN characteristics that determine the overall performance of h-BN-based energy platforms.

The bulk form of h-BN possesses a wide bandgap of 5.6–5.9 eV [24,25]; however, the surface/edge functionalization of its nanostructures or doping with external chemical species has proved effective in modulation of its bandgap. As an example, fluorine-doped 2D h-BN shows a large reduction in bandgap (from 5.8 to 3.1 eV) and consequently a semiconductive behavior [26]. This bandgap reduction occurs mainly through the formation of defect states, between the highest occupied molecular orbital (HOMO) and lowest unoccupied molecular orbitals (LUMO). [27]. Depending on the type of external chemical species on 2D h-BN lattice, the defect/dopant energy states are located either close to the HOMO (acceptors) or LUMO (donors). Hence, the 2D h-BN can be converted to a synthetic semiconductor by controlled doping, defect engineering, and grafting functional groups, commonly based on oxygen [28,29] or carbon [5,30]. The high intrinsic mechanical strength of 2D h-BN followed by enhanced conductivity through functionalization could be used to stabilize different commercial battery electrolytes or membranes in fuel cells. In fact, the change in surface local energy of 2D h-BN by variation of surface chemical composition can lead to higher proton exchange rates, ionic conductivity, and catalytic activity, developing a suitable platform for energy applications. Accordingly, a wide range of h-BN properties, from surface chemistry to optical transparency, will influence the performance of h-BN-based energy devices (Figure 1d).

The synthesis process of 2D h-BN nanomaterials is also crucial in determining their chemical/physical properties. This could be done either by inducing reactions between B- and N-rich precursor materials to generate h-BN flakes (bottom-up) or breaking the h-BN layered structure apart to form nano- or micro-sized flakes (top-down) [31]. The former methods are often employed to produce atomically thin 2D h-BN or when surface charge uniformity is important (i.e., photonics or solar cells) [32]. For instance, chemical vapor deposition (CVD) has shown to be a promising technique to produce homogeneous large area h-BN layers. Nevertheless, the need for expensive equipment, stoichiometric sensitivity of product (formation of side products -B_xN_y), and lack of control on selective functionalization are the challenges hindering the wide integration of CVD in 2D h-BN synthesis for energy applications [33].

The latter, however, has been extensively used to prepare the 2D h-BN nanomaterials for energy applications due to their cost-effectivity, easy manipulation of the surface/edge chemistry, dispersibility in diverse liquid and solid media, and high production yield [34,35]. The top-down processes are often carried out in liquid media, an example of which is liquid-phase exfoliation (LPE). Thus far, multiple LPE techniques, such as bath ultrasonication [36], probe sonication [37], ball milling [38], hydrothermal [39], solvothermal [40], and microwave-assisted exfoliation [41] were developed to obtain 2D h-BN with controllable size, thickness, and surface functionalization. In an LPE process, the solvent's molecules/ions facilitate the h-BN exfoliation by diffusing into spaces between two adjacent layers. Hence, depending on the exfoliation media the extent of liquid/h-BN interactions and product yield change [42]. Lewis acid-base interactions, Columbic interactions, and polar covalent bonding are the three main pathways for a liquid medium to interact with the h-BN. In either case, upon functionalization, the doping level and electronic properties of the 2D h-BN change [43]. Considering the importance of these surface functional groups and doping level in energy applications, exfoliation or synthesis parameters should be carefully selected. So far, functionalization with the hydroxyl group [-OH] [44], amine group [-NH_2] [45], long change molecules [46,47], and doping with carbon [48], fluorine [49], and oxygen [50] have been largely used to modify 2D h-BN. Table 1 provides a summary of 2D h-BN synthesis for energy applications. The detailed information on the synthesis methods, parameters, and structural analyses of h-BN nanomaterials can be found in References [7,14].

Table 1. Summary of advantages and drawbacks of 2D h-BN synthesis methods for application in energy devices.

	Process	Advantages	Disadvantages	Ref.
Top-down	Sonication	• Cost effectiveness • High exfoliation yield by probe sonication • Various synthesis media • Controllable size and thickness • Surface/edge functionalization • Scalability	• Structural defectivity • Uncontrollable side reactions • Low exfoliation yield with bath-sonication	[36,37]
	Ball milling	• Providing both wet and dry synthesis environments • Surface/edge functionalization	• High degree of defectivity • Long synthesis process • Edge oxidation • Lack of reproducibility	[38]
	Hydrothermal/ Solvothermal	• High exfoliation yield • Controllable size and thickness • Surface/edge functionalization • Scalability • Rapid and energy-efficient process • Reproducibility	• Solvothermal processes may lead to toxic byproducts • Need for high temperature and pressure • Need for PTFE equipped Autoclave	[39,40]
	Microwave	• Fast process • Reproducible • Dry and wet synthesis media	• Complex design • Uncontrolled side reactions	[41]
Bottom-up	Hydrothermal/solvothermal	• Accurate control over the size and thickness • Synthesis of BNQDs, BNNRs, BNNSs • Selective edge functionalization • Controlled in-situ doping with external atoms • Low temperature and pressure	• Solvothermal processes may lead to toxic byproducts • Need for PTFE equipped Autoclave • Need for 1:1 B:N stochiometric ratio in precursors	[51,52]
	CVD (AP, PE, LP)	• Applicable for direct deposition on various substrates • High uniformity in large scale • High quality flakes • Controllable lateral size, thickness, and surface stochiometric ratio • High conformality	• Costly equipment • Low deposition rate • Need for pre- and post-annealing processes • Toxic by-products	[53–55]

PTFE: Polytetrafluoroethylene; BNQDs: Boron Nitride Quantum Dots; BNNRs: Boron Nitride Nano Ribbons; AP: Ambient pressure; PE: Plasma Enhanced; LP: Low Pressure.

This review covers the recent advancements in the application of 2D h-BN nanomaterials in various energy sectors with a focus on interfacial interactions that improve the performance of 2D h-BN in different energy storage/conversion devices. To this end, we demonstrate the importance of surface modification for harnessing the full applicability of 2D h-BN. Electrochemical energy production/storage systems including fuel cells, batteries, and supercapacitors, together with thermoelectric and photovoltaic applications of 2D h-BN will be discussed, followed by examining the future trends, obstacles, solutions, and possibilities in the integration of 2D h-BN in energy applications.

2. Application of 2D h-BN

2.1. Batteries

2.1.1. Li-Ion Batteries (LIBs)

Application of 2D h-BN in Li-ion batteries can be roughly categorized into three main sections: (1) electrode materials, (2) separators and (3) electrolytes [56–59]. It is known that the major drawbacks of conventional anodic electrodes, such as lack of safety at higher power densities or inadequate theoretical capacitance (i.e., 372 $mAh.g^{-1}$ for graphite) can be addressed by the incorporation of materials with high swift charge/discharge rates (e.g., 2D h-BN) into the battery [60,61]. To harness the full capability of 2D h-BN,

it is often hybridized with other materials. As an example, hybridization of only 2 wt.% 2D h-BN with reduced graphene oxide (r-GO) has demonstrated a high reversible capacity of 278 mAh g^{-1}, a current density of 100 mA g^{-1} with improved cycling stability up to 200 cycles [62]. In fact, the synergistic effect of the 2D h-BN/r-GO interface generated by van der Waals forces minimizes the interlayer volume expansion caused by Li-ion intercalation on the electrodes. Similarly, the enhanced polarization of the anode electrode of lithium titanium oxide/r-GO hybridized with 2D h-BN demonstrated almost two times lower charge transfer resistance compared to when 2D h-BN was not present. In 2D h-BN/silicene heterostructures, the formation of intermediate complexes at interface decreases the bandgap (to 1.85 eV), Li^+ binding energy, and Li^+ diffusion barrier [62]. With these advantages, the maximum capacity of the unit can reach 1015 mAh g^{-1}. Besides the bare 2D h-BN, functionalized structures of 2D h-BN with various oxygen-based functional groups have also shown reversible charge/discharge surface reactions with Li-ions, revealing specific capacity up to 78 mAh g^{-1} with good Coulombic efficiency for an electrode (Figure 2a) [43,63].

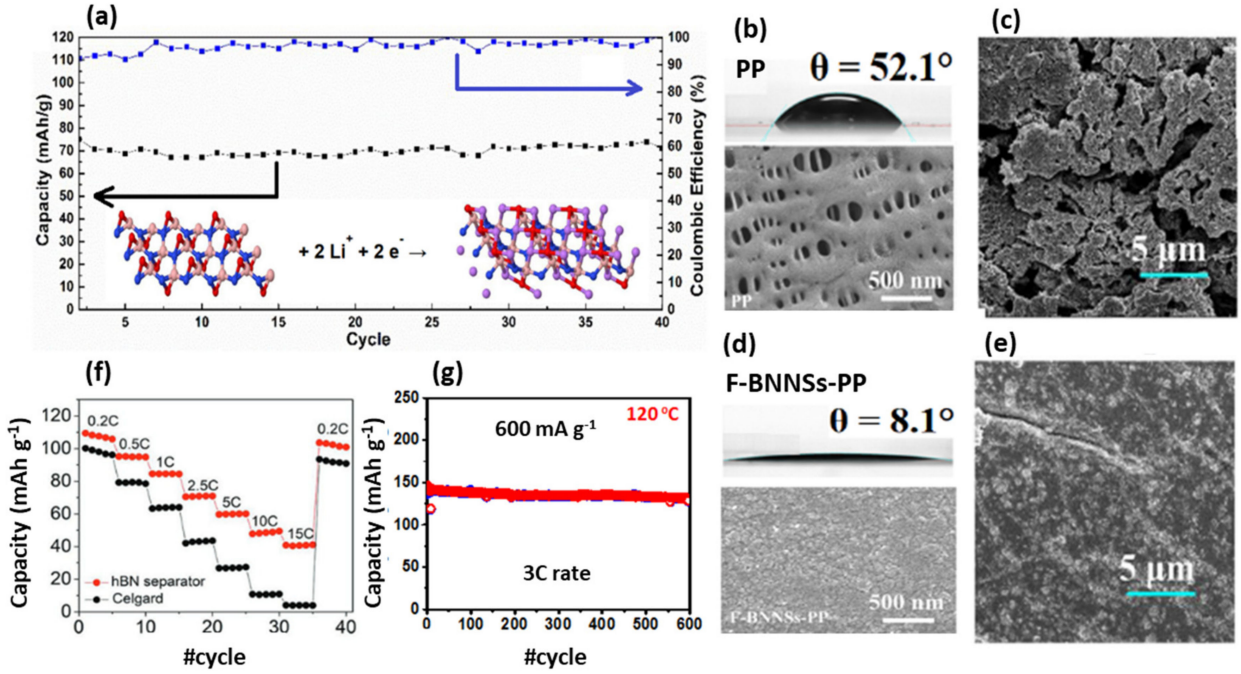

Figure 2. (**a**) Cyclic performance and Coulombic efficiency of FBN (inset: one possible redox energy storage mechanism for FBN) (Reprinted with permission from Royal Society of Chemistry, Copyright © 2016). Electrolyte-separator contact angle and top-view SEM images of the (**b**,**c**) PP and (**d**,**e**) F-BN-PP separator, respectively [64] (Reprinted with permission from American Chemical Society, Copyright © 2021). (**f**) rate capability of the LMO-graphene||Li cell at 0.5 C and from 0.2–15 C, respectively [65] (Reprinted with permission from WILEY-VCH, Copyright © 2019). (**g**) Cyclic stability curve of lithium titanite (LTO) half-cells assembled based on 2D h-BN-based electrolyte at 120 °C after 600 cycles [66] (Reprinted with permission from WILEY-VCH, Copyright © 2016).

Electrode separation is another major application of 2D h-BN in LIBs. The presence of a separator, a physical barrier between the electrodes, is vital to prevent short circuits and control ion migration during charge-discharge cycles [65,67]. The short circuit of a LIB often derives from uncontrolled battery overheating. Then, a thermally stable separator can improve the operability and decrease safety concerns [68]. The common separators such as polypropylene (PP) and polyethylene (PE) suffer from low wettability against liquid electrolytes and uneven Li^+ diffusion flux [69,70]. On the contrary, 2D h-BN with local surface polarities exhibits a uniform flux distribution of Li^+ as a separator, and the ionic conductivity of the electrolyte was shown to improve (from 0.160 to 0.255 mS m^{-1}) [69].

More importantly, 2D h-BN suppresses the formation of Li-dendrites. The Li-dendrites formed by uncontrolled growth of Li on the anodes can penetrate through the separator and cause short circuits in LIB. As seen in Figure 2b, the SEM images of the PP separator's morphology demonstrates large pore sizes on the surface, leading to higher impedance resistance. The surface morphology of the PP separator after 100 cycles at the current density of 5 mA cm^{-2} also demonstrates the extreme distribution by Li-dendrites and gaps (Figure 2c). The SEM images of 2D h-BN modified PP separator before and after the same charge-discharge cycles (shown in Figure 2d,e, respectively) show that the addition of 2D h-BN suppressed the growth of dendritic morphology and presented a smoother surface [64]. Further research on improvement of commonly used separators with h-BN nanomaterials such as boron nitride nano tube (BNNTs)/PP [71], PE/PP/PE modified 2D h-BN [67], PE-BN/poly (vinylidene fluoride-hexafluoropropylene (PVDF-HFP) [67] established 2D h-BN as a vital component for separators' proper operation. The polymer-free blade coated 2D h-BN was also employed as the separator in Li-manganese oxide/graphene/2D h-BN/Li cells, exhibiting a capacity retention of 82% after 100 cycles (Figure 2f) [65]. In fact, the proper deposition and growth of the 2D h-BN layer resulted in an excellent separation performance as a sole matrix.

As discussed, 2D h-BN improves the electrolyte performance in two ways: (1) enhancing the mechanical stability and fabrication robustness, and (2) increasing the ionic conductivity and Li transference number ($t_{Li}{}^{+}$). Generally, to increase the mechanical stability of electrolytes, the gel polymer electrolytes (GPE) or gel ionic electrolyte (GIE) are used instead of liquid electrolytes and reinforced by inorganic fillers such as TiO_2 or Al_2O_3 [72–75]. However, these fillers act as a barrier against ion transport and affect the overall cell capacity. In contrast, 2D h-BN provides both mechanical strength and ionic conductivity (upon functionalization) at the same time and can potentially address this issue [1]. It was demonstrated that the addition of only 0.5 wt% perfluoropolyether (PFPE) modified 2D h-BN into P(VdF-co-HFP) increases the $t_{Li}{}^{+}$ from 0.41 to 0.63 while the electrolyte shear modulus (G) is enhanced five times [73]. Similarly, the addition of bulky h-BN into LiTFSI/1,3-dioxolane (DOL)-1,2-dimethoxymethane (DME) [76–78], amino-functionalized 2D h-BN into trimethylolpropane triacrylate (TMPTA) with PVDF-HFP [79], and 2D h-BN/polyacrylonitrile (PAN) into LiPF in EC/ethyl methyl carbonate (EMC) [80] demonstrated exceptional increase in both $t_{Li}{}^{+}$ and G. Moreover, the thermal stability of the GPE and GIE is enhanced by incorporation of 2D h-BN. Accordingly, the addition of 2D h-BN and bentonite into LiTFSI/1-methyl-1-propyl piperidinium bis (trifluoro methyl sulfonyl) imide (PP13) is shown to maintain a capacity of 90 $mAhg^{-1}$ at 120 °C for almost 20 days (Figure 2g) (more than 600 cycles) while 2D h-BN-free electrolyte malfunctions above 60 °C [66].

2.1.2. Mg Metal-Based Batteries (MMBs)

MMBs batteries with an electrode potential of −2.37 V propose a high theoretical capacity of 2250 $mAhg^{-1}$ [81]. Along with the electrochemical properties, the abundance of Mg in nature makes it a competitive candidate for use in the secondary batteries market. One serious obstacle in way of commercializing these batteries is the insertion/extraction of Mg into the cathode due to the highly polarized nature of Mg^{2+} ions [82]. Fluorine functionalized 2D h-BN nanomaterials were reported to be well-functioning cathodes in MMBs [83]. The cyclic voltammetry (CV) graphs shown in Figure 3a indicate that Mg^{2+} ions are successfully intercalated on the edge sites of the 2D h-BN, resulting in an anodic peak at 1.75 V. The de-intercalation also occurs with a cathodic peak at 0.8 V while pristine 2D h-BN does not show any redox reaction. The calculated current density from the CV is 48 mAg^{-1}, and the discharge capacity after 80 cycles is 50 $mAhg^{-1}$. In contrast, the undoped 2D h-BN does not show a good electrochemical behavior (Figure 3b). As seen in electrochemical impedance studies (EIS) (Figure 3c), the semi-circles in high and medium frequency regions are attributed to the solid electrolyte interphase (SEI) and charge transfer resistance, respectively. The linear trend at the low-frequency region displays the

Warburg impedance correlated with ion diffusion resistance. The calculated R_{SEI} (SEI resistance) of undoped and doped 2D BN is 128 Ω and 94 Ω, respectively. Similarly, R_{ct} (charge transfer resistance) illustrates a considerable drop of 34% from 209 Ω for undoped BN cathode to 137 Ω for doped 2D h-BN. Therefore, it can be concluded that the doping of 2D h-BN with fluorine enhances the conductivity of the electrode. The footprint of this improved behavior in the doped 2D h-BN cathode is also observed in Figure 3d [83]. As seen, by increasing the charge/discharge cycles, the discharge capacity of doped 2D h-BN is raised continuously and reaches a maximum value of 50 $mAhg^{-1}$ at 80 cycles. In another study, a graphene/2D h-BN composite was used as the cathode material and the nominal composition of graphene /20 wt.% 2D h-BN revealed the best performance with a current density of 25 mAg^{-1} and discharge capacity of 105 $mAhg^{-1}$ (75 mAg^{-1} and 94 $mAhg^{-1}$ for bare graphene cathode, respectively) up to 80 cycles [81]. The excessive increment of 2D h-BN content deteriorates the performance of the battery due to its insulative characteristics. The implementation of a few-layer MoS_2 cathode, compared to 2D h-BN, demonstrated better capacity (170 $mAhg^{-1}$); however, the electrode stability was limited to only 50 cycles [84]. Although the electrochemical performance of the Mg-ion batteries is improved by addition of 2D h-BN, the mechanisms by which these improvements occur are not yet well understood.

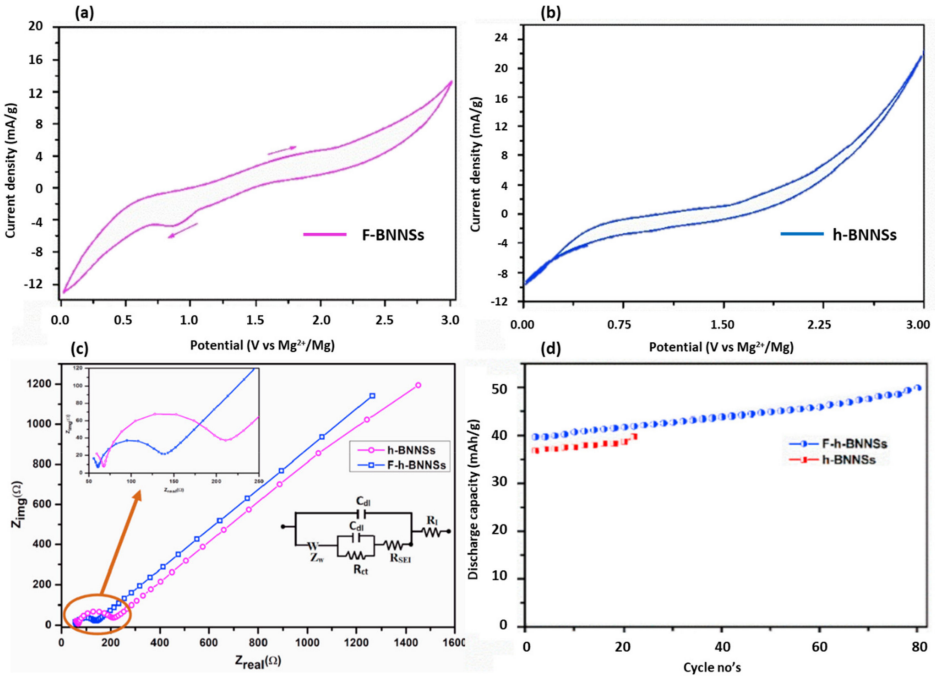

Figure 3. CV plots at a scan rate of 5 mVs^{-1} in the voltage range of 0.0–3.0 V (**a**) F doped 2D h-BN and (**b**) undoped 2D h-BN cathodes (**c**) Impedance spectrum of doped and undoped 2D h-BN cathodes, (**d**) Cycle life of doped and undoped BN cathodes [83] (Reprinted with permission from Elsevier B.V, Copyright © 2019).

2.1.3. Zinc Flow Batteries (ZFBs)

ZFBs are often considered to be reliable energy storage systems for stationary applications owing to their high energy density, cost-effectivity, and safe operation [85]. Despite these advantages, the scaled-up production and commercialization of these batteries are still lacking. One of the limiting factors is the zinc dendrite/accumulation, deteriorating the cycle-life of the batteries. This process is greatly influenced by the inhomogeneous temperature distribution on the electrode as well as the poor mechanical characteristics of the membrane [86]. Thus far, many efforts have been devoted to obviating these shortcomings, using 2D h-BN. The incorporation of 2D h-BN into ZFBs is made through three major pathways: (1) modification of the electrolyte chemistry, (2) reinforcing membranes, and (3) changing the battery configuration [87,88].

Recently, Hu and coworkers exploited a porous polyether sulfone membrane coated with 2D h-BN in an alkaline zinc-iron flow battery [89]. Based on the obtained results, 2D h-BN acts as a heat transporter when facing the anode, modifies the morphology of zinc, and reinforces the membrane. According to the voltage-time diagrams, the bare membrane was stable up to 40 h (Figure 4a), followed by a fluctuation due to the formation of zinc needle-like dendrite penetrating through the membrane and micro-short circuiting. This dendrite formation may also damage the membrane, leading to the crossover of the electrolyte. As a result, self-discharge and declining concentration of the active materials occur. The sharp rise of voltage in the final step pertains to this concentration polarization, since the potential of the Fe $(CN)_6^{3-}$/Fe $(CN)_6^{4-}$ depends on the concentration of the electrolyte. Accordingly, the discharge capacity decreases considerably. In contrast, the 2D h-BN coated membrane demonstrates an outstanding performance with voltage stability after 500 cycles (800 h) (Figure 4a). The proposed mechanism is such that 2D h-BN helps the generated heat distribute uniformly in favor of the facile plating/stripping of zinc on the electrode. In addition, 2D h-BN strengthens the membrane against the damage induced by the non-uniform deposition of zinc when the battery is charging. Supreme Coulombic efficiency (CE) of 98.5% and energy efficiency (EE) of 87.6% after 500 cycles support the proposed mechanisms (Figure 4b). The 2D h-BN-based battery has reached the highest ever reported efficiency of 80% after 200 cycles among all ZFBs (Figure 4c) [90,91].

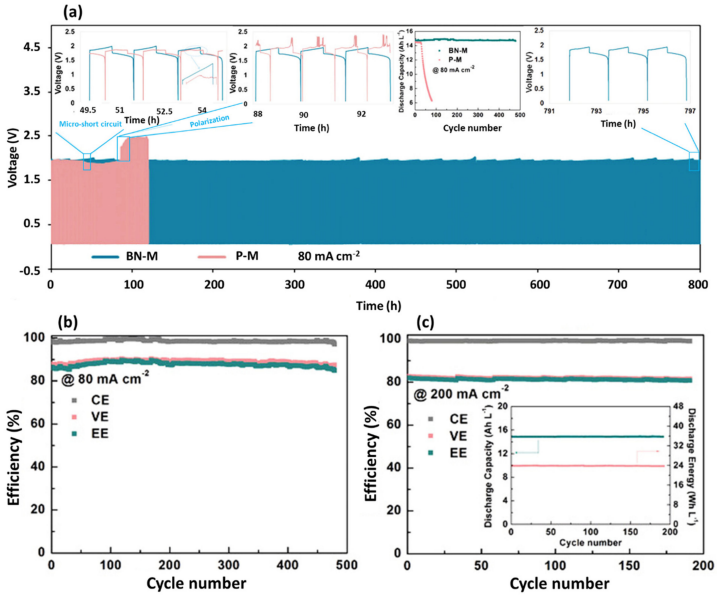

Figure 4. (**a**) Voltage-time profiles of the alkaline zinc-iron flow batteries using BN modified membrane and pristine membrane at a current density of 80 $mAcm^{-2}$. Cycling performance of the alkaline zinc-iron flow battery assembled with BN-M at the current density of (**b**) 80 $mAcm^{-2}$ (**c**) 200 $mAcm^{-2}$. Inset: the corresponding discharge capacity and discharge energy for each cycle [89] (Reprinted with permission from WILEY-VCH, Copyright © 2020).

2.1.4. Other

In recent years, the abundance of Na and K resources and their lower costs as compared to Li have drawn attention to Na and K ion batteries. The storage mechanism in these batteries is to some extent similar to that of LIBs [43]. However, under the same weight, the volume of Na or K ions is considerably larger than that of Li and therefore, the energy density is much lower [43]. These drawbacks have considerably suppressed the extensive application of Na and K ion batteries. Similar to what was discussed in the Section 2.1.1, 2D h-BN was also incorporated in sodium ion batteries' (NIBs) design. For instance, 2D h-BN was demonstrated to be an effective capping agent for black-phosphorene (Pn) as an anode material of NIBs [92]. By h-BN modification, the anode performance was improved significantly due to

enhanced binding energy of Na in the h-BN/black-Pn heterostructure (2.55 eV) compared to pristine Pn (1.59 eV). Moreover, the Na-ion barrier movement within the layers was reduced by the incorporation of 2D h-BN. Apart from that, the silicene/2D h-BN heterostructure was theoretically shown to be an ultrafast ion diffusion anode material due to the enhanced binding strength of Na on 2D h-BN [92]. Focusing on the wide bandgap of 2D h-BN and the possibility of band gap modification after the formation of vacancies and absorption of Na^+ and K^+ ions, monolayer h-BN can be a great candidate for an anodic material [93]. Accordingly, the storage capacities, open-circuit voltages, and energy densities of 571.698 mAh/g, 0.0099 V and 5.656 Wh/ kg can be obtained for h-BN reinforced NIBs [94,95]. A comparison of battery performance improvement by incorporating 2D h-BN is shown in Table 2.

2.2. Supercapacitors

Supercapacitors have recently been in high demand for energy storage due to their peculiar characteristics of high-power density, swift charge/discharge capability, and better safety records and a long-life cycle in comparison to batteries [106,109]. Over the last decade, 2D h-BN nanostructures (i.e., functionalized and/or doped ones) and their heterostructures have been introduced as promising inorganic materials to improve the performance of supercapacitors [35,110–112]. The 2D h-BN modifications can generate available free electrons or enhance the mobility of the charge carriers in order to improve the electrochemical behavior [113–116]. Moreover, the partial polarity of the B-N bonds facilitates the charge separation within the 2D h-BN lattice. In fact, 2D h-BN demonstrates a pseudocapacitive behavior owing to this partial ionic character of the B-N bonds. In addition, the oxidation state of B and N atoms can be changed through intercalation with the electrolyte during the redox reaction, contributing to additional charge storage. Combining electrochemical double-layer capacitance (EDLC) with such pseudocapacitive materials amplifies the energy density and the specific capacitance. Furthermore, functionalization of 2D h-BN can introduce additional acceptor and donor electronic states depending on the functional group, resulting in more efficient energy storage.

2.2.1. Electrodes

Electrodes are the most crucial parts of a supercapacitor assembly. Therefore, most of the research on 2D h-BN-based compounds has been dedicated to the improvement of the electrodes' performance. As one of the earliest attempts, Gao et al. developed a 2D h-BN/r-GO nanocomposite electrode with the capacitance of 140 F g^{-1}, almost 75% higher than that of a bare r-GO electrode [102]. The capacitance of 2D h-BN/r-GO increased by 5.5% after 1000 cycles, indicating the high stability of 2D h-BN/r-GO, and attributed to the hindrance of r-GO sheets agglomeration. In a similar study, various 2D h-BN/r-GO architectures were prepared and their electrochemical behavior in different stoichiometric ratios was evaluated [104]. By increasing the GO proportion from 0.1 g (named h-BNG1) to 0.4 g (named h-BNG4) in the primary batch containing 0.3 g boric acid and 0.3 g urea, a superlattice architecture was obtained (Figure 5a,b). Additionally, the electrochemical behavior of the composite electrode changed from Faradic to EDLC. The formed superlattice structure led to an incremental increase in electrical conductivity through carrier confinement within the graphene pathways embedded in the h-BN domains and increasing π conjugations. The electronic work function of the composite was also reduced from 296 (in h-BNG1) to 22 meV (in h-BNG3). Cyclic voltammetry tests, shown in Figure 5c, revealed that h-BNG1 possesses a low specific capacitance of 218 F g^{-1} at a scan rate of 20 mV s^{-1} (could be attributed to 2D h-BN as the dominant phase). The potential window of h-BNG2 is located at both negative and positive areas (−0.5–0.5 V), and the curves show distorted features, indicating that the storage mechanism was neither EDLC nor pseudocapacitive (Figure 5d). This behavior could be due to insufficient intercalation between r-GO and 2D h-BN nanosheets since the generation of the active sites depends on the intercalation process. The highest specific capacitance was recorded for h-BNG3 with 960 F g^{-1} at a scan rate of 10 mV s^{-1}, pertaining to the synergistic effect of the EDLC and pseudo capacitance as well as the presence of more active sites on the superlattice structure of the electrode (Figure 5e).

Table 2. Device performance of energy storage units (batteries and supercapacitors) based on 2D h-BN.

Application	Platform	Device Characteristic	Role of 2D h-BN	Ref.
LIB	h-BN/r-GO	Reversible capacity of 278 mAh/g Current density of 100 mA/g 200 cycle stability	Electrode	[62]
LIB	LTO/rGO/h-BN	Increased specific capacity to 200 mAh/g high capacity of 179 mAh.g^{-1} at a discharge rate of 20 C Ultrafast charge rate of >10 C.	Electrode	[96]
LIB	2D h-BN/blue phosphorous	The low diffusion energy barrier of Li (0.08 eV) High theoretical specific capacity of 801 mAh/ g	Electrode	[63]
LIB	h-BN/silicene	Storage capacity of 1015 mAh/ g Low volume change (only 1.3%)	Electrode	[97]
LIB	BNNSs modified PP separator in a $LiFePO_4$ ‖ Li full cell	Reducing separator's contact angle from 52.1 to 8.1 Enhanced ionic conductivity to 0.255 mS/m Excellent long cycling performance (82% retention after 800 cycles) High current density (100 mA cm^{-2} in 800 h)	Separator	[64]
LIB	BNNTs modified PP separator in a $LiFePO_4$ ‖ Li cell	Enhanced dimensional stability at 150 °C Li diffusion coefficient of 4.7×10^{-8} cm^2/s High charge/discharge current rates of 5–10 C	Separator	[71]
LIB	h-BN flakes in PE-BN/PVDF-HFP bilayer separator in a $LiFePO_4$ ‖ Li	Low thermal shrinkage (only 6.6 %) at 140 °C Rapid electrolyte uptake of 348% Low R_{ct} of 6.67 Ω The superior capacity retention of 95% after 500 cycles	Separator	[67]
LIB	2D h-BN ink separator in Li-manganese oxide (LMO)-graphene ‖ Li (anode)	The capacity retention of 82% after 100 cycles Highly stable at 150 °C	Separator	[65]
Li-S	Celgard 2400 separator/functionalized h-BN flakes containing CO_3^{2-}	The capacity retention of 91.5% at the high rate of 7 C Cyclic stability up to 1000 cycles	Separator	[98]
Li-S	BNNSs/PP	Improved ionic conductivity to 1.35 mS/cm Inhibiting dendrite nucleation The initial capacity of the PP-BNNSs (1405 mAh/g) Withstanding a high temperature of 80 °C for 1 min	Separator	[99]

Table 2. *Cont.*

Application	Platform	Device Characteristic	Role of 2D h-BN	Ref.
LIB	(PFPE)-h-BN into P(VdF-co-HFP) (PVH) polymeric	High t_{Li}^{+} = 0.62 Improved shear modulus (G) (5.2 times higher) Nearly 1940 h working hours	Electrolyte	[73]
Li-S	2D h-BN in LiTFSI/1,3-dioxolane (DOL)—1,2-dimethoxymethane (DME) liquid electrolyte	High t_{Li}^{+} = 0.55 Nearly 400 h constant working hours Deep plating up to 35 mAh/cm High mechanical stability of the electrolyte	Electrolyte	[77]
LIB	Amino-functionalized h-BN (AFBN)-based GPE in $LiFePO_4$ | | Li	Enhanced ionic conductivity of 6.47×10^{-4} S/cm Enhanced t_{Li}^{+} = 0.23 compared to h-BN free electrolyte (0.12) Cell retaining up to 92%	Electrolyte	[79]
LIB	Carbon/ h-BN in imidazolium ion liquids electrolyte	Excellent ionic conductivity (>1 mS/cm) Shear storage modulus (5 MPa) t_{Li}^{+} value can be as high as 0.18 (200% improvement) Compatible with high-voltage cathodes (>5 V vs. Li/Li^{+}) Working temperature up to 175 °C	Electrolyte	[100]
NIB	h-BN/Blue P	Theoretical specific capacity of 541 mAh/g Low diffusion barrier of 0.07 eV	Electrode	[43]
NIB	Monolayer h-BN	The theoretical capacity of 571.698 mAh/g The average electrode potential of 0.009 V	Electrode	[94]
MMBs	F-doped h-BN Celgrade as a separator with Mg $(ClO_4)_2$ [DBIm]Br	The good discharge capacity of 50 mAh/g Improved conductivity	Electrode	[83]
ZFBs	BNNSs	500 cycles at 80 mA/cm^2 Efficiency up to 80% at 200 mA/cm Working temperature up to 50 °C Columbic efficiency (CE) of 96.03% Voltage efficiency (VE) of 90.21%	Membrane	[89]
ZFBs	Sulfonate functionalized BNNSs	Long term stability (2500 h at 2 mAh/cm^2) Small plating/stripping overpotential of 45 mV Cyclic stability up to 1200 cycles	Electrode	[101]
Supercapacitor	h-BN/rGO	The capacitance of 140 F/g (75% higher than bare r-GO electrode) Excellent cyclic stability (105.5% capacitance retention after 1000 cycles)	Electrode	[102]

Table 2. *Cont.*

Application	Platform	Device Characteristic	Role of 2D h-BN	Ref.
Supercapacitor	$ZnCo_2S_4$ (ZCS)/h-BN/CNT/polypyrrole	The specific capacitance of 534 and 785 F/g in aqueous and organic media, respectivel Excellent cycling stability of 106% (after 10,000 charge/discharge cycles) in aqueous electrolyte	Electrode	[103]
Supercapacitor	h-BN/rGO	The specific capacitance of 960 F/g. Energy and power density of 73 Wh/kg and 14,000 W/kg, respectively. High stability (~80%) even after 10,000 cycles	Electrode	[104]
Supercapacitor	Zn-CdS/h-BN/CNT	The specific capacitance of 787 F/g The energy density of 78 Wh/kg High stability (99%) even after 10,000 cycles.	Electrode	[105]
Supercapacitor	h-BN/graphene	The specific capacitance of 322 F/g Energy and power density of 44.7 Wh/kg and 3588 W/kg, respectively. Good stability (96%) even after 6000 cycles.	Flexible electrode	[106]
Supercapacitor	h-BN/PANI/CNT	The specific capacitance of 515 F/g The energy density of 46 Wh/kg High stability (98%) even after 10,000 cycles.	Electrode	[107]
Supercapacitor	Sulfonated polysulfone/h-BN/ionic liquid	Proton conductivity of 1.3×10^{-3} S/cm at 100 The specific capacitance of 90.4 F/g Energy and power density of 43.8 Wh/kg and 1100 W/kg, respectively. High stability (98%) even after 10,000 cycles.	Electrolyte additive	[108]

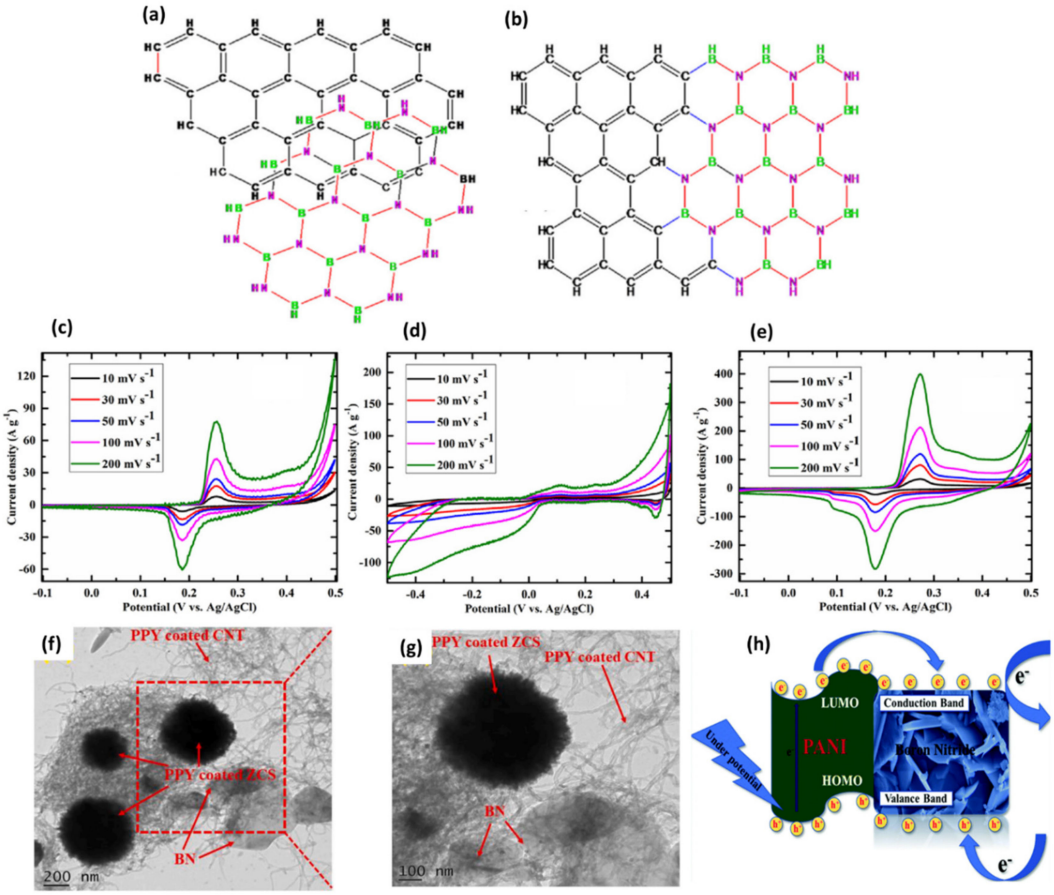

Figure 5. The atomic framework of (**a**) h-BNG2 and (**b**) h-BNG3. CV of (**c**) hB-NG1 (**d**) h-BNG2, and (**e**) h-BNG3 at different scan rates [104] (Reprinted with permission from Elsevier B. V, Copyright © 2017). TEM images of ZCS/BN/CNT/PPY at (**f**) lower and (**g**) higher magnification [103] (Reprinted with permission from Elsevier B. V, Copyright © 2020). (**h**) Schematic of the probable electron transfer mechanism within PANI and BN under an applied potential [107] (Reprinted with permission from Royal Society of Chemistry, Copyright © 2020).

2D h-BN has also been employed in a quaternary composite of $ZnCo_2S_4$ (ZCS)/2D h-BN/CNT/Polypyrrole (PPY) as a high-performance electrode (Figure 5f,g) [103]. Considering the poor cycling stability of bare ZCS, the combination of ZCS with other pseudocapacitive materials including 2D h-BN and PPY will overcome this problem. This often occurs through stabilization of the system with the assistance of π-π interactions and Coulombic attractions, leading to a remarkable increment in the active sites for electrochemical interactions. This complex geometry exhibited high specific capacitance of 534 and 785 F g^{-1} in aqueous (1 M KCl) and organic (1 M $TEABF_4$ in acetonitrile) media, respectively.

Surface functionalization is an alternative approach for the incorporation of 2D h-BN into supercapacitor electrode designs. However, due to surface charges, 2D h-BN sheets tend to agglomerate; therefore, hybridization with other nanostructures or conducting polymers is required. Recently, hydroxyl (-OH) functionalized 2D h-BN/polyaniline (PANI)/CNT nanohybrid was employed as an electrode [107]. It was shown that 2D h-BN stabilizes PANI in the system via a Coulombic interaction. Then it reduces the agglomeration tendency of CNTs through charge surface blocking mechanism and minimization of surface interactions. Moreover, the surface area was enhanced from 50.49 m^2/g to 89.77 m^2/g due to the homogeneous deposition of PANI on CNTs and the diffusion of fiber-like PANI decorated CNTs into the 2D h-BN.

This nanohybrid electrode showed a specific capacitance of 515 F g^{-1} and cyclic stability of 98% after 10,000 charge/discharge cycles. The proposed mechanism for electron transfer is illustrated in Figure 5h. Under an applied potential, the PANI's LUMO interacts with the conduction band of 2D h-BN, and leads to a reduction in the LUMO energy of PANI and the conduction band of h-BN. In addition, an electron is transferred from the PANI's HOMO to LUMO and then the conduction band of h-BN. The presence of oxygen functional groups on the 2D h-BN surface is shown to facilitate this interaction owing to the additional acceptor and donor levels of the electronic states [22]. A higher specific capacitance of 787 F g^{-1} in a 1 M KCl solution is recorded for the Zn-CdS/2D h-BN/CNT electrode compound in which the crystallization of flower-like nanostructures by oxygen functionalized 2D h-BN and CNTs resulted in this outstanding performance (Figure 6a) [105]. Brunauer–Emmett–Teller (BET) measurements also showed that introducing 2D h-BN leads to more than 60% enhancement in specific surface area (from 151 m^2/g to 246 m^2/g).

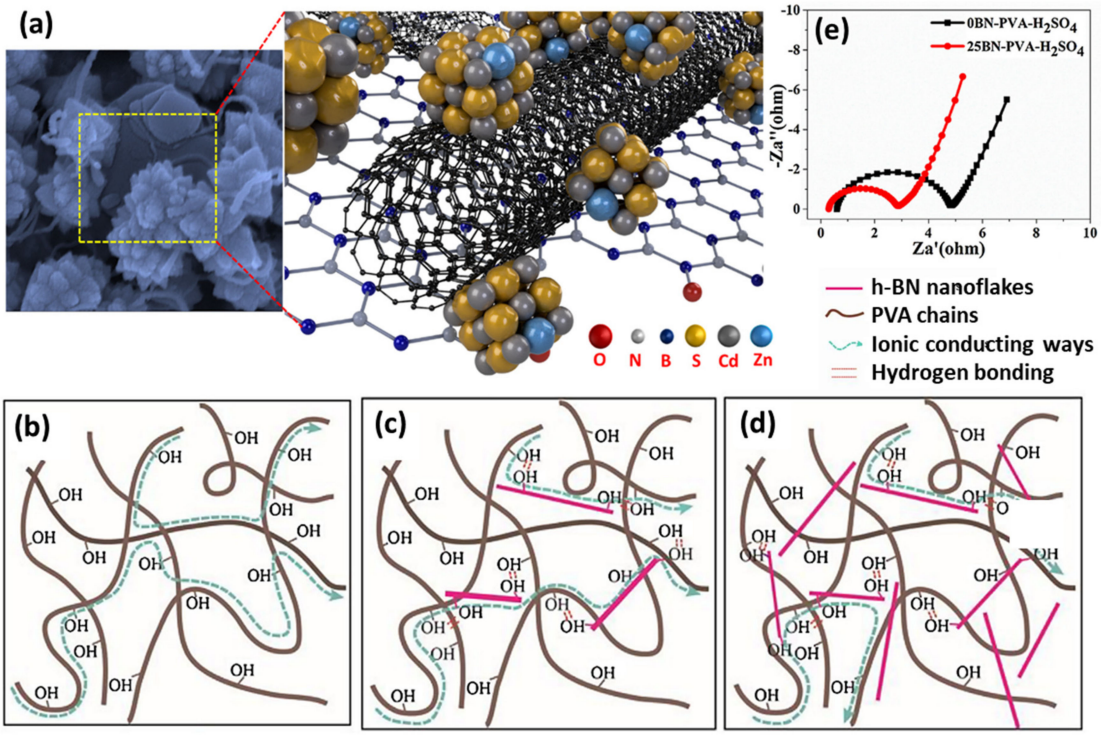

Figure 6. (**a**) Schematic representation of the cathode matrix with functionalized boron nitride sheets, carbon nanotubes, and Zn-doped CdS nanoparticles along with a FESEM image [105]. (Reprinted with permission from Elsevier B. V, Copyright © 2021). Illustration of ionic conduction process for (**b**) ions conduction along the twisted PVA chains, (**c**) proper amount of 2D h-BN leading to direct conduction of ions and (**d**) an excessive amount of 2D h-BN hindering the conduction of ions (**e**) EIS of supercapacitors with 0 and 25% h-BN-PVA-H_2SO_4 GPE [117] (Reprinted with permission from Elsevier B. V, Copyright © 2017).

2.2.2. Electrolyte

Improvement of electrolyte performance in both mechanical and thermal aspects can be achieved by the incorporation of 2D h-BN [108]. It has been reported that by adding only 0.025 mg ml^{-1} h-BN the ionic conductivity of PVA-H_2SO_4 GPE increases from 9 to 29 mS cm^{-1} [117]. Since the charge carriers in PVA-H_2SO_4 (H^+) transport by hopping mechanism between hydrogen bonds, an optimal amount of 2D h-BN launched swift ion transportation through its functional groups. An excessive amount of 2D h-BN caused restacking of the nanosheets and obstructed the ion movements (Figure 6b–d) [117]. As seen in the EIS graphs in Figure 6e, the presence of a small semi-circle at the high-frequency

region and the slope at the low-frequency end represent an ideal EDLC behavior [117]. It should be noted that the first intersection of the curve with Z' demonstrates the bulk resistance of the supercapacitor, the diameter of the semi-circle represents the charge transfer resistance of the electrode, and the slope corresponds to the diffusion resistance in the supercapacitor. Accordingly, it can be inferred that supercapacitors containing 2D h-BN have lower charge transfer resistance due to the emergence of the ionic highways. This high ionic conductivity and mechanical stability of 2D h-BN drew the researchers' attention towards the applicability of 2D h-BN as a separator of a solid-state planar asymmetric supercapacitor [118].

2.3. Thermoelectrics

Considering the increasing importance of green energy production, thermoelectric materials converting heat to electricity have become an area of great interest [119–121]. To characterize the thermoelectric conversion efficiency via the material-dependent figure of merit, Equation (1) is used:

$$ZT = \frac{\sigma S^2 T}{K_e + K_{ph}} \quad (1)$$

where σ, S, T, K_e, and K_{ph} represent the electrical conductivity, Seebeck coefficient, absolute temperature, and electronic and phononic thermal conductivity, respectively [122,123]. Therefore, a large Seebeck coefficient and electrical conductivity, and a small thermal conductivity are in favor of high-performance thermoelectric devices. However, the interdependence of the Seebeck coefficient, and electrical and thermal conductivity are serious challenges in thermoelectric materials research, as changing one parameter could adversely affect the other two in any given compound. According to Equation (1), the electrical insulation and high phonon conductivity of h-BN suppress the ZT value [124–126]. Nevertheless, introducing defects to the h-BN structure and hybridization with other 2D materials could enhance its thermoelectric properties [127]. In a theoretical study, the figure of merit of zigzag and armchair h-BN nanoribbons (ZBNNRs and ABNNRs) were compared with that of zigzag and armchair graphene nanoribbons (ZGNRs and AGNRs) [128].

The diagrams of phonon thermal conductance with respect to the absolute temperature of the 2D h-BN system are shown in Figure 7a. As seen, when T is almost 0 K, the thermal conductance approaches $3K_0$, attributing to contributions from three acoustic phonon modes. By raising the temperature, the thermal conductance is enhanced due to the activation of higher modes. In wider ribbons (Figure 7b), the enhancement of the thermal conductance becomes more apparent owing to higher accessible channels for phonon transport [128]. Calculations in Figure 7e,f suggest that ABNNRs demonstrate the best thermoelectric performance of all, with a maximum figure of merit of about 0.2. Moreover, the value of ZT can be tailored by introducing lattice defects in the ribbons, whose positions highly affect the ZT, as depicted in Figure 8a,b.

Although the thermoelectric properties of h-BN nanomaterials are improved by introducing structural defects, their values are still not high enough to be used in real devices. One leading approach to address this issue is to assemble h-BN heterostructures with graphene and other 2D materials [130,131]. With very high electrical conductivity, graphene could be a good option for thermoelectric applications; however, its high thermal conductivity needs to be tailored to obtain an acceptable ZT value [132]. Although graphene and h-BN represent high in-plane thermal conductance, their cross-plane conductance is low, deemed to be an advantage for thermoelectric devices. To explore the thermoelectric transport properties at the interface of graphene and h-BN [133], Raman spectroscopy is often used to apply a temperature gradient between the top and bottom graphene layers. Considering the zero lateral temperature gradients, the diagram of thermoelectric voltage as a function of the cross-plane temperature gradient shows a linear trend, resulting in a Seebeck coefficient of -99.3 μV/K. The obtained result is nearly two times higher than that of single-layer graphene at room temperature (50 μV/K) [134]. The calculated power factor is ~1.51×10^{-15} W/K^2, offering a quite low value due to the insulating character-

istics of h-BN. Indeed, a thick enough h-BN layer would diminish quantum mechanical tunneling, whereas both electron tunneling and thermionic emission across the energy barrier contribute to the cross-plane Seebeck coefficient [135,136]. Finally, a low value of 1.05×10^{-6} was calculated as the figure of merit of the device, which is due to the thick h-BN layer, and consequently, the large energy barrier at the interface of graphene/h-BN (0.5 eV). By tailoring the energy barrier height and the thickness of h-BN, higher ZT values can be achieved [137,138]. A remarkable enhancement of ZT up to 0.7 was also predicted theoretically in superlattice armchair ribbons consisting of graphene and h-BN sections [139]. However, the insulating behavior of h-BN causes a high electron scattering and shifts the maximum ZT values to higher chemical potentials. Further improvement of phonon scattering in these heterostructures requires complex simulations to understand the transport phenomena at graphene/2D h-BN interfaces [129]. For instance, Figure 8c,g demonstrates h-BN flakes periodically attached to armchair graphene nanoribbons. In this case, phonon thermal conductance is diminished while electronic conductance is almost conserved. Moreover, introducing 2D h-BN causes bandgap broadening, leading to an increment of the Seebeck coefficient. In this situation, the ZT value will increase from 0.6 for a short heterostructure system (n_{BN} = 1) to 0.81 for longer systems (n_{BN} > 5). Interestingly, these high ZT values are predicted for small and achievable chemical energy levels of around 0.4 eV. In addition, introducing vacancies in the central region of graphene layers may increase the ZT up to 1.48 at room temperature, mainly due to extra suppression of phonon conductance [129].

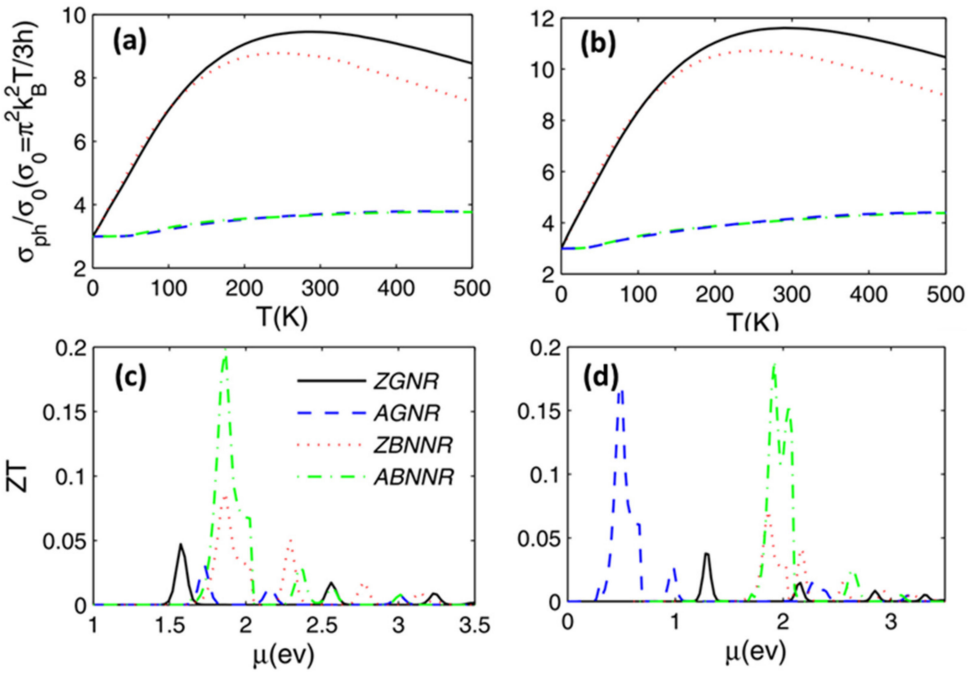

Figure 7. (**a**,**b**) Phonon thermal conductance K_{ph}/K_0 as a function of the temperature T. (**c**,**d**) figure of merit ZT as a function of the chemical potential μ. [128] In the left columns (**a**,**c**), $N_A(N_Z)$ = 8, while in the right columns (**b**,**d**), $N_A(N_Z)$= 10. (Reprinted with permission from AIP Publishing, Copyright © 2013).

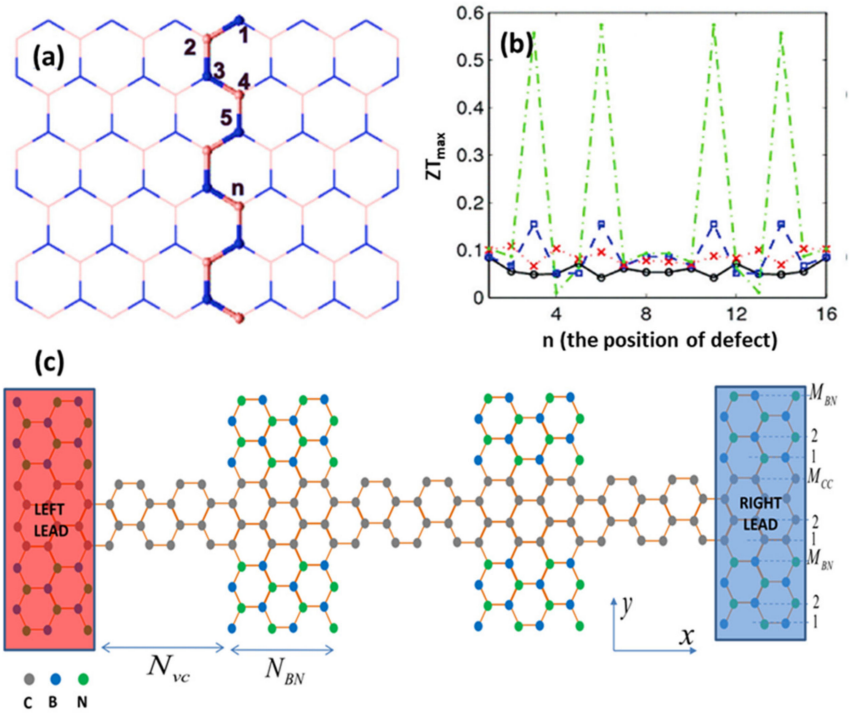

Figure 8. Schematic of ZBNNR (**a**) with different defect sites to be considered, which are labeled by the number 1, 2, 3, n. (**b**) The ZT max as a function of the position of defect n for $N_A(N_Z) = 8$. The solid, dashed, dotted, and dotted dashed curve corresponds to the ZGNR, AGNR, ZBNNR, and ABNNR, respectively [128] (Reprinted with permission from AIP Publishing, Copyright © 2013). (**c**) Schematic view of graphene/BN heterostructure with subsections made of BN flakes attached to the main AGNR channel. The two leads are made of BN/G/BN ribbons as the hybrid parts of the active device [129] (Reprinted with permission from IOP Publishing, Ltd., Copyright © 2015).

Doping the G/h-BN heterostructure with chemical species can also impact the ZT, as witnessed in the case of tetrathiafulvalene (TTF) and tetracyanoethylene (TCNE) doped G/2D h-BN heterostructures. TCNE, as an electron acceptor, causes the Fermi level to shift between the valence band of the ribbon and its LUMO. In contrast, TTF as an electron donor leads to observing the Fermi level between the conduction band of the ribbon and HOMO of TTF (Figure 9a) [140]. The Fermi level shift triggers a notable increment of the thermopower and electronic figure of merit. Moreover, the presence of dopants in the structure leads to extra phonon scattering. Accordingly, ZT of 0.1 and 0.9 were predicted for TCNE and TTF doped graphene/2D h-BN.

Recently, it was shown that heterostructures of 2D h-BN and 2D GeP_3 can be promising thermoelectric materials [141]. Pristine GeP_3 depicts supreme charge carrier mobility and good chemical stability; however, its small bandgap degrades the thermoelectric characteristics. It is noteworthy to mention that the higher bandgap values for GeP_3 can be obtained in mono and bilayer structures due to the dominance of quantum confinement; however, no reports on their experimental synthesis have been published so far. One approach to enlarge the band gap of GeP_3 is capping 2D h-BN layer as an insulating material, preserving the in-plane electrical conductance of GeP_3. As illustrated in Figure 9b–e, GeP_3 is an indirect bandgap material with E_g of 0.23 and 0.12 eV for monolayer (1L) and bilayer (2L) GeP_3, respectively [141]. These values increase to 0.34 eV when a monolayer 2D h-BN is inserted. However, the number of 2D h-BN layers is not of paramount importance regarding the band structure. Evaluations unveiled that p-type GeP_3/BN 1_1 (i.e., monolayer GeP_3 and monolayer 2D h-BN) with a doping level of 0.004 e/u.c, could have a maximum ZT of 5.13 at room temperature (Figure 9f). In absence of experiential research, thersitical studies

suggest that controlled integration of 2D h-BN into thermoelectric materials and devices can open pathways for explorations in this field in the net future [136,137].

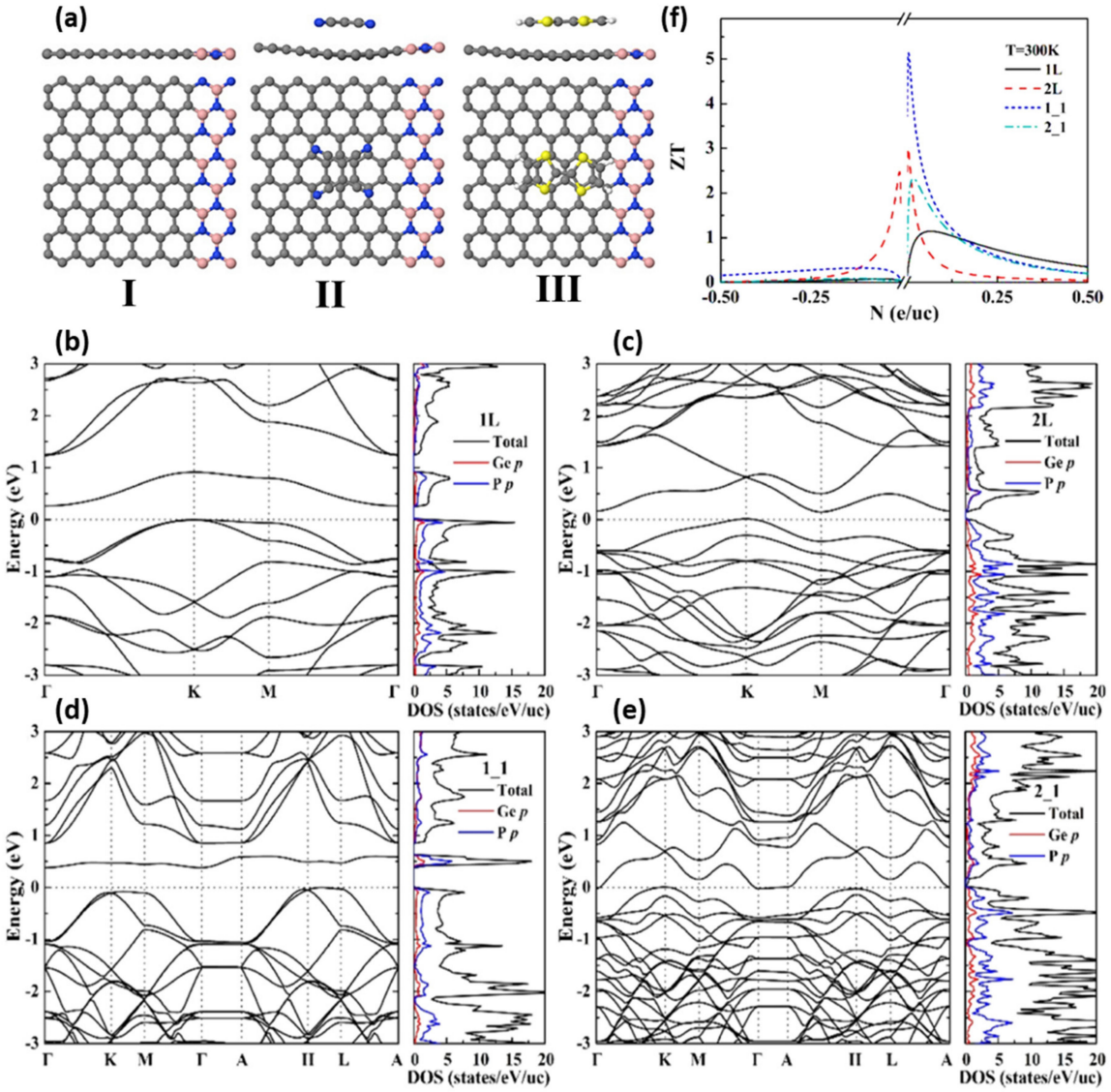

Figure 9. (**a**) Side and top views of graphene/2D h-BN heterostructures (I) without doping, (II) doped by electron acceptor-TCNE, and (III) doped by electron donor-TTF [140] (Reprinted with permission from IOP Publishing, Ltd., Copyright © 2015). (**b**,**c**) Calculated band structure and corresponding DOS for 1L and 2L GeP_3, respectively. (**d**,**e**) Calculated band structure and corresponding DOS for GeP_3/h-BN m_1 heterostructures (m = 1 and 2), respectively. (**f**) ZT values for 1L and 2L GeP_3, as well as for GeP_3/h-BN m_1 heterostructures (m = 1 and 2) [141] (Reprinted with permission from American Chemical Society, Copyright © 2021).

2.4. Fuel Cells

2.4.1. Membrane

Direct methanol fuel cell (DMFC), as an essential member of the fuel cells family, faces some technical problems, e.g., passing of methanol through the polymer electrolyte membrane (PEM), slow methanol oxidation and oxygen reduction reactions. The methanol crossover reduces the efficiency of DMFCs by the creation of a mixed potential at the cathode. The undesired oxidation, decreasing the active sites for reduction of oxygen at the cathode, and carbon monoxide poisoning of the cathode catalyst are other methanol crossover challenges [142–145]. Nafion, as the most common PEM used in DMFCs, suf-

fers from the methanol crossover despite its supreme proton conductivity and outstanding chemical, thermal, and mechanical stability [146–148]. One attempt to decrease the methanol crossover in Nafion is to use 2D h-BN as reinforcement. Polarized covalent bonds of B and N lead to valence electron accumulation around the N atom and create an uneven distribution of electron cloud, resulting in high proton conductivity. This high proton conductivity along with its large surface area, low density, thermomechanical stability, barrier effect, and excellent chemical resistance, make 2D h-BN a great candidate as a PEM filler employed in DMFCs. For this purpose, 2D h-BN can be functionalized via -OH groups to escalate the side-chain reactions with -mercaptopropyl trimethoxysilane to form continuous ionic channels in the PEM. The proton conductivity of bare Nafion improved from 135 to 214 mS.cm^{-1} after adding 0.75wt.%BN. The mechanism is explained through the formation of–SO_3H groups in the functionalized 2D h-BN. At the same time, the methanol crossover is reduced by the addition of 2D h-BN in the membrane [149]. Considering the ratio of the proton conductivity and methanol crossover current density, the electrochemical selectivity of Nafion/0.75wt.%BN can be as high as 6.63×10^{-2} S/mA compared to 1.81×10^{-2} S/mA in pristine Nafion. This composite membrane exhibits a high peak power density of 165 mW/cm^2 at 70 °C, which is much higher than that of pristine Nafion (65 mW/cm^2) [149].

Regarding the high cost of the Nafion, many researchers actively examine other alternatives, including poly(2, 6-dimethyl-1,4-phenylene oxide) (PPO) owing to its high T_g, as well as mechanical and hydrolytic stability [150]. The transport behavior and remarkable hydrophobic/hydrophilic phase separation of Sulphonated PPO (sPPO) renders outstanding electrochemical performance [151]. However, since a higher degree of sulfonation might reduce its stability, incorporating different additives would be beneficial [152]. Covalent functionalization of h-BN with the hydrophilic acidic group makes them well-dispersed in the sPPO matrix [153]. Experimental results show that adding 5 wt.% sBN can result in 168 % increase in Young's modulus of sPPO. This large increase is attributed to $\pi - \pi$ interactions between sBN and sPPO. Moreover, availability of more sulfonic acids in sPPO/sBN and the formation of hydrogen bonding with water molecules, the water sorption of the sPPO/sBN was 50.61%, almost 50% higher than that of bare sPPO. The proton conductivity was also enhanced by 67% in sPPO/sBN due to the presence of excess sulfonic acid groups and hydrogen bonding bridges, introducing long-range proton-conducting pathways. In this case, vehicular and Grotthuss mechanisms were suggested for the proton conduction. In the vehicular mechanism, protonated water molecules in the forms of $H_3O^+{}_{aq}$, $H_5O_2{}^+{}_{aq}$, and $H_9O_4{}^+{}_{aq}$ diffuse through the media and act as ion transport carriers, whereas the latter mechanism deals with the stationary water molecules in which ion hopping occurs from one water molecule to another through hydrogen-bonded ionic channels [43]. Figure 10a depicts how sBN simplifies proton conduction by the vehicular and Grotthuss mechanisms. A low methanol permeability of 2.04×10^{-7} cm^2/s was also obtained in sPPO/sBN, which is significantly lower than sPPO and Nafion (three and nine times, respectively). This is due to interfacial interactions of sPPO and sBN, as well as the barrier effect of sBN owing to its 2D structure, which hinders the methanol crossover [153]. Moreover, the overall performance of the cells indicated a high peak power density of 122 mW/cm^2 for sPPO/sBN, which is two times higher than that of sPPO. In another survey, a polyether ether ketone (PEEK) membrane reinforced with polyaniline coated activated boron nitride (PANI-BN) was used to improve the performance of DMFC [154]. Although the addition of PANI-BN improved the performance of the membrane, it was not as high as the results obtained from sPPO/sBN. For instance, the best results for SPEEK/0.1 wt.% PANI-BN membranes were a water uptake of 58 %, proton conductivity of 4.13 mS/cm, methanol permeability of 3.08×10^{-7} cm^2/s, and power density of 11.38 mW/cm^2.

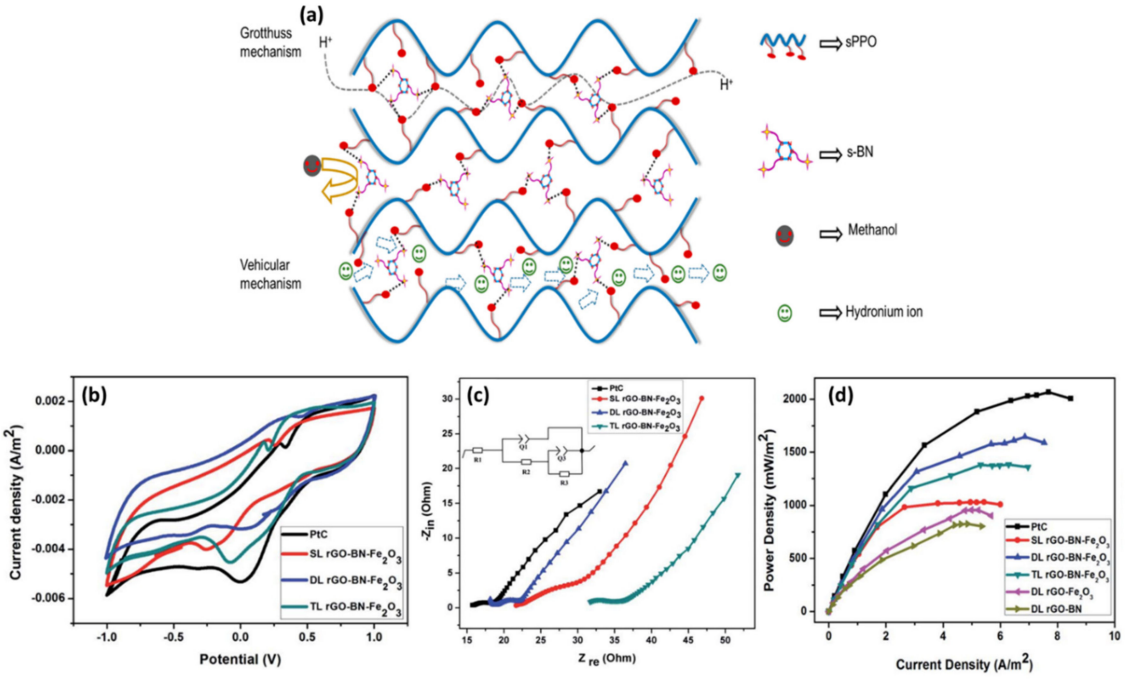

Figure 10. (**a**) Schematic representation of composite membranes illustrating the methanol crossover resistance (by sBN) and improved proton conductivity by adding sulfonic acid groups of sBN by hopping and vehicular mechanism [153] (Reprinted with permission from American Chemical Society, Copyright © 2020). (**b**) cyclic voltammetry and limiting current (derived from cyclic voltammograms) of the MFCs with rGO–2D h-BN–Fe_2O_3 (SL, DL, and TL) hybrid nanocomposite cathodes. EIS spectrum of (**c**) PtC and rGO–2D h-BN–Fe_2O_3 (SL, DL, and TL). (**d**) Power density curves of the MFCs produced with different cathodes and PtC catalyst loadings, along with the rGO–2D h-BN–Fe_2O_3 hybrid nanocomposite and rGO–2D h-BN and rGO–Fe_2O_3 composite [155] (Reprinted with permission from Royal Society of Chemistry, Copyright © 2020).

2.4.2. Cathode Catalyst

Although 2D h-BN can participate in catalytic reactions [14], there are not many reports on 2D h-BN being employed in fuel cell electrodes. Recently, a novel nanostructure of rGO-2D BN-Fe_2O_3 was introduced as the cathode catalyst of a microbial fuel cell (MFC) [155]. The concept is based on the insertion of 2D h-BN and Fe_2O_3 onto the r-GO nanosheets to enhance the surface area for facile transport of reactants and improve electron transport to graphene. The CV graphs in Figure 10b indicate that the limiting current of the double-layer (DL) in r-GO-2D h-BN-Fe_2O_3 electrode is higher than that of the single (SL) and trilayer (TL) (5.5 mA, 4.9 mA, and 4.4 mA, respectively); however, it was lower than that of Pt/C (5.9 mA). The superior limiting current of DL is described by the larger surface area and electrical conductivity of r-GO and 2D h-BN nanosheets. The EIS evaluations also confirm that Pt/C cathode has better performance since its correlated semicircle in the high-frequency area has a smaller diameter than that of rGO-BN-Fe_2O_3 (Figure 10c). Power density measurements of the cells also reveal that rGO-BN-Fe_2O_3 is a promising cathode catalyst for MFCs with a power density of 1673 mW/m^2, which is 81% of the obtained power density for MFC using Pt/C cathode (Figure 10d) [155]. All in all, the abundance and cost effectiveness of this new cathode material makes it a competitive catalyst compared to other conventional ones.

2.4.3. Hydrogen Environmental Barrier Coating

A new application of 2D h-BN in fuel cells is the hydrogen environmental barrier coatings (EBCs), which hinder the hydrogen diffusion and embrittlement of materials. Studies revealed that hydrogen embrittlement can occur in fuel cells working at tempera-

tures up to 1273 K [156]. In addition to preventing embrittlement, it is necessary to retain hydrogen fuel. The deposition method and obtained microstructure significantly affect the effectiveness of 2D h-BN barriers. For instance, employing ion beam assisted deposition can form (002) planes oriented orthogonal to the substrate, not capable of preventing H_2 diffusion [157]. Radiofrequency magnetron sputtering, however, results in barriers with considerably lower permeability of H_2 [158]. Deposition of h-BN flakes parallel to the substrate demonstrated remarkable outcomes by trapping H_2 as stable bubbles up to 1073 K [159]. Recently, atomic layer deposition (ALD) was exploited to deposition 2D h-BN onto ZrO_2 powders to evaluate their high temperature H_2 diffusion behavior [160]. ALD can provide low defect density thin films that are strongly bonded to the substrate [161]. Figure 11a shows TEM images of a thin 2D h-BN layer of 2.4 nm deposited onto ZrO_2. The stability of h-BN at high temperatures was evaluated by exposing bulk BN powder to 20% H_2 in Ar balance for three hours at 1773 K. Almost all the N contents of the 2D h-BN lattice remained intact, which can be explained by the high N vacancy formation energy of 5.6 eV at elevated temperatures [160].

2.4.4. Seal

Another novel application of 2D h-BN in fuel cells is as a compressive seal in a solid oxide fuel cell (SOFC). A 2D h-BN/glass nanocomposite formed by tape casting method was used as a practical sealing material, where the sealing phenomenon occurs gradually through running thermal cycles [162]. The reported leakage rates decreased to less than half after only 10 thermal cycles under different input gas pressure, as shown in Figure 11b. Figure 11c illustrates the structure of seals after one thermal cycle. This porous structure explains the high leakage rate. Conversely, Figure 11d displays a denser microstructure formed after 10 thermal cycles. Finally, more tests revealed that a liquid B_2O_3 film was formed on the 2D h-BN surface over time at elevated temperatures shown schematically in Figure 11e–g.

2.5. Solar Cell

Solar photovoltaic technology is considered to be mainstream renewable technology with a great potential to generate clean, reliable, scalable, and affordable electricity [163]. However, from the materials engineering point of view, as regards circuit design, many issues still need to be resolved [164]. In this regard, 2D layered materials have been in the forefront of solar cell industry due to their unique electrical and optical properties [165]. Nevertheless, 2D materials-based solar cells performance might be disturbed by environmental conditions such as certain gases and humidity, signifying the need for protective layers. In the last decade, scientists have used 2D h-BN in various solar cells to passivate the surface of active materials or design the interface of heterojunction solar cells. The peculiar characteristics such as lack of dangling bond, large bandgap, excellent chemical and thermal stability, excellent crystallinity, medium dielectric constant, and easy transfer to substrates without affecting its bulk properties make 2D h-BN a top candidate for this application [166–168].

In a research study, 2D h-BN was used as a passivation layer on top of a MoS_2/WSe_2 van der Waals heterojunction solar cell to decrease the cell's electrical loss [169]. As a result, the average recombination lifetime of the electron-hole increased from 112 ps to 131 ps, indicating the reduced recombination rate at the active area as well as leakage path passivation. Thus, the charge diffusion length and charge extraction rate were enhanced. Recently, 2D h-BN has been introduced as a promising passivation layer for InP as a high-performance III-V semiconductor. Raj et al. [170] exploited five and seven-layer thickness of 2D h-BN to passivate InP solar cells in order to reduce the recombination phenomenon caused by the surface defect states (Figure 12a–c). The calculated number for the interface defect density was 2×10^{12} $eV^{-1}cm^{-2}$, which is better than the results of other passivation layers such as Al_2O_3, HfO_2, and SiO_2 with interface defect density of 2.6×10^{12} $eV^{-1}cm^{-2}$, 5.4×10^{12} $eV^{-1}cm^{-2}$, and 5×10^{12} $eV^{-1}cm^{-2}$, respectively [171,172]. In addition, by

introducing 2D h-BN on InP, the efficiency, V_{OC}, J_{SC}, and fill factor (FF) of the solar cell increased from 11.5% to 17.2%, 0.72 V to 0.78 V, 27.4 $mAcm^{-2}$ to 29.4 $mAcm^{-2}$, and 58.6% to 75.2%, respectively. They postulated that the surface passivation occurred through charge transferring from the surface defect states of InP to 2D h-BN, which made them inactive. Notably, they demonstrated that the passivation is dependent on the thickness of 2D h-BN. This thickness dependence is due to a quantum mechanical tunneling current which is directly proportional to the charge carrier density at the dielectric/semiconductor interface (h-BN/i-InP), and inversely proportional to the thickness of the dielectric layer and band offsets. Accordingly, a thinner 2D h-BN leads to higher J_{sc}, while a thicker one decreases the tunneling current, attributing to lower contact recombination, lower dark current, and ultimately higher V_{oc} (Figure 12d).

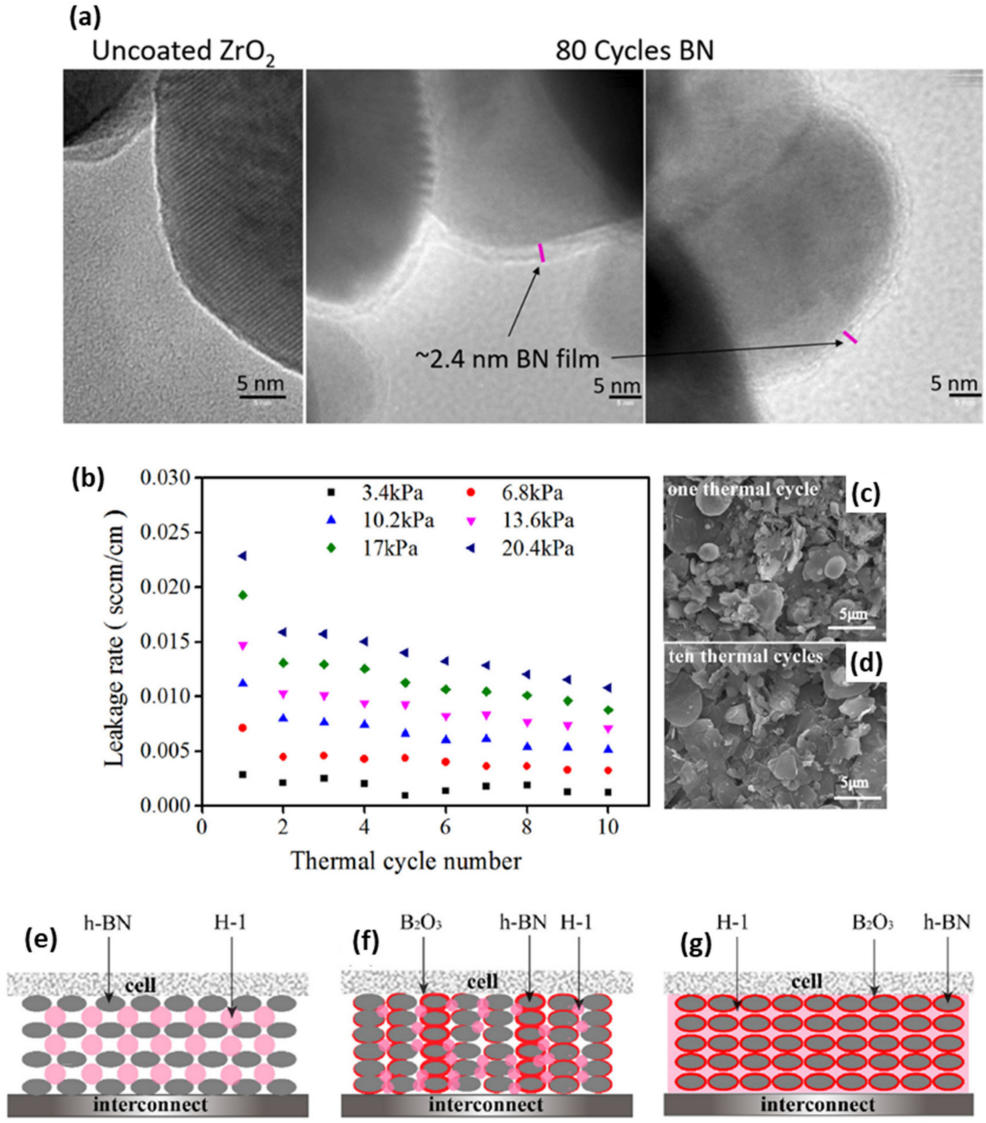

Figure 11. (**a**) TEM micrographs of uncoated ZrO_2 and ZrO_2 coated with ~2.5 nm amorphous BN film deposited using 80 ALD cycles. The leakage rates of BH60 seals after ten thermal cycles under a compressive load of 0.2 MPa and different input gas pressures at 750 °C [160] (Reprinted with permission from Elsevier B.V, Copyright © 2021) (**b**) SEM micrographs of BH60 seal after (**c**) one thermal cycle and (**d**) 10 thermal cycles. (**e**–**g**) Schematic diagrams of the microstructure evolution of the BH60 seals overtime at 750 °C [162] (Reprinted with permission from Elsevier B.V, Copyright © 2020).

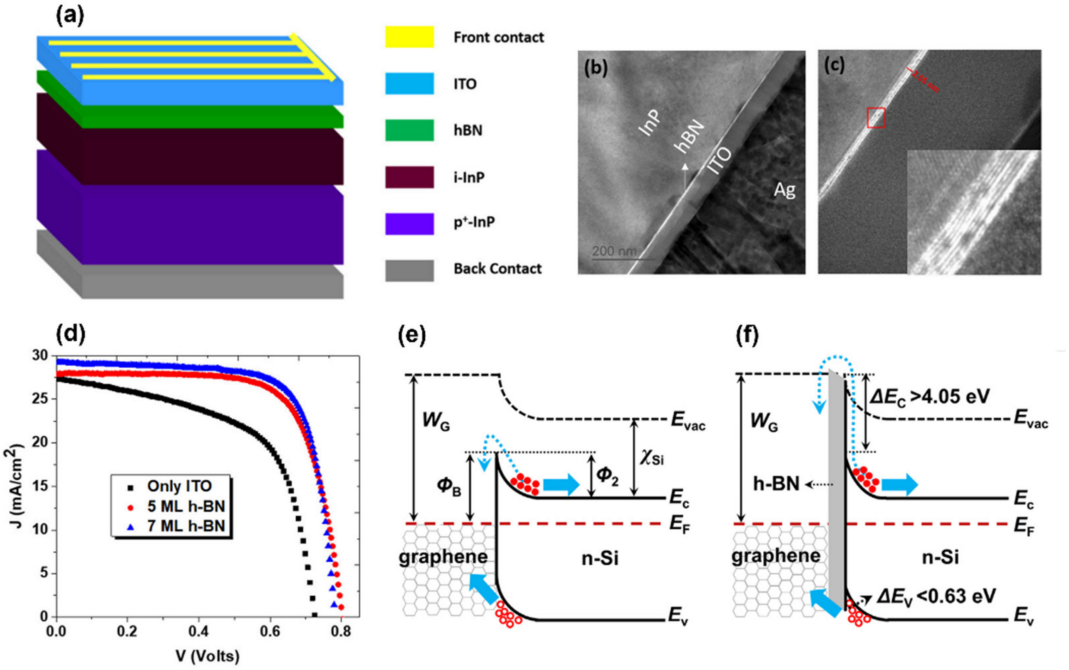

Figure 12. 3D schematic and TEM of the device structure. (**a**) A schematic showing different layers of a solar cell with 2D h-BN. (**b**) A cross-sectional TEM image of the solar cell showing different layers (scale bar: 200 nm). (**c**) A magnified TEM image showing 2.55-nm thick h-BN sandwiched between ITO and i-InP (scale bar: 20 nm). Inset shows the layered structure of h-BN. (**d**) J−V characteristics of a f the 2D h-BN-InP solar cell with and without 2D h-BN layer measured under AM 1.5 G illumination [170] (Reprinted permission from Springer Nature, copyright © 2021). Energy band diagrams of the Gr/Si Schottky junction solar cells (**e**) without and (**f**) with an h-BN electron blocking layer [173] (Reprinted with permission from Elsevier B.V, Copyright © 2016).

Exploiting 2D h-BN as a passive layer can be considered a milestone for InP since the lack of lattice-matched and wide bandgap passivation layer was a limiting factor for its development. Except for passivation of heterostructure solar cells, 2D h-BN has been employed in dye-sensitized solar cells (DSSCs) to passivate the anode (TiO_2 nanoparticles). The anode material in DSSC should provide a high surface area in order to host a large number of photoactive dye molecules [174]. However, by increasing the surface area of TiO_2, the number of surface states increases, leading to higher rates of recombination [175]. Moreover, the heat treatment of TiO_2 at temperatures around 450 °C to form the anatase phase which is favorable for DSSC, leads to the formation of oxygen vacancies [176]. Consequently, there will be more surface deficiencies deteriorating the cell's performance. Therefore, a passivation layer is necessary to reduce the surface energy and hinder the recombination of electron-holes by introducing an energy barrier. Oxide ceramics with high-k dielectrics are conventional candidates for the passivation of TiO_2. However, there are several critical issues associated with them, i.e., poor conformal coverage over a large area, blocking photo-generated electrons from the dye due to relatively high thickness, and reducing the porosity of TiO_2 [177]. In contrast, an ultrathin and high crystalline layer of h-BN can be deposited on TiO_2 to modify its semiconducting behavior. It was reported that by applying a 2D h-BN layer on TiO_2 the J_{SC}, V_{OC} and efficiency of the DSSC were enhanced by 23%, 1.6%, and 57%, respectively, meaning well suppression of the surface states at the TiO_2/electrolyte interface [178].

Another application of 2D h-BN in solar cells is interface engineering for heterojunction structures. Schottky junction solar cells, such as graphene/Si, have become popular due to their high potential for inexpensive photovoltaic applications [179]. However, their low Schottky barrier leads to the interface recombination of charge carriers that remarkably

suppresses their efficiency. One effective way to address this issue is to insert an insulating 2D material between graphene and Si. Accordingly, 2D h-BN would be an ideal candidate for this application. In a study on graphene/h-BN/Si solar cell platforms [173] it was shown that 2D h-BN can hinder the diffusion of electrons (majority carrier) from n-Si to graphene, and the transport of holes (minority carrier) from n-Si to graphene. Based on the band alignment demonstrated in Figure 12e, without a 2D h-BN interlayer, the built-in electric field at the interface causes the separation of photogenerated electron/hole pairs and pulls the electrons to n-Si, whereas holes drift towards graphene. Simultaneously, the built-in electric field hinders the diffusion of electrons from n-Si to graphene (dashed line in Figure 12e,f). However, the small surface potential of n-Si (Φ= 0.6–0.7 eV) will become smaller under light irradiation. The inevitable consequence of this would be a significant current leakage [173]. By introducing 2D h-BN to the system, the unwanted recombination will be reduced since the conduction band offset (ΔEC) of h-BN/Si is larger than 4.05 eV, meaning there is a large obstacle for electron transport from n-Si to graphene. On the other hand, the small valence band offset (ΔEV) of 0.63 eV facilitates the drift of holes from n-Si to graphene under the built-in electric field, which is an essential factor to prevent an increase in the series resistance of cells. Hence, the reverse saturation current density was significantly reduced from 4.09×10^{-3} mA/cm^2 to 2.56×10^{-4} mA/cm^2 for graphene/Si and graphene/h-BN/Si, respectively. Using 2D h-BN in other heterostructure solar cells such as MoS_2/h-BN/GaAs [180] and graphene/h-BN/GaAs [181] has also improved the interface characteristics in a similar approach. Table 3 provides a summary of energy conversion devices based on 2D h-BN.

Table 3. Comparison of energy conversion device performance based on 2D h-BN.

Application	Platform	Role of 2D h-BN	Device Characteristics	Mechanisms	Ref.
Thermoelectrics	h-BN nanoribbons	Direct conversion of temperature difference to the electric voltage.	ZT = 0.2 at a chemical potential of 1.8 eV.	-	[128]
Thermoelectrics	Graphene/h-BN/graphene heterostructures	Heat dissipation across the graphene/h-BN junction.	Seebeck coefficient of -99.3 μV/K, power factor of 1.51×10^{-15} W/K^2, and ZT of 1.05×10^{-6}	A large energy barrier at the interface caused a low ZT	[133]
Thermoelectrics	Graphene/h-BN hetero-nanoribbon doped with TTF	Acting as a tunnel barrier	Phonon thermal conductance of 0.2 nW/K, thermopower of -284 μv/K, and ZT of 0.9 at room temperature	Introducing additional phonon scattering by doping the structure and decreasing the phonon conductance.	[140]
Thermoelectrics	Graphene/h-BN heterostructures	Band gap opening in graphene	ZT = 1.48	Increase in the phonon scattering andreduction the phonon thermal conductance	[129]
Thermoelectrics	GeP_3/h-BN heterostructures	Enlarging the bandgap of GeP_3.	An ultrahigh ZT value of 5.13 at 300 K in p-type GeP_3/h-BN.	Increase in the bandgap of GeP_3 followed by the formation of an anisotropic electronic structure with a higher ZT.	[141]
Fuel cell	Nafion/h-BN	Reinforcement of the polymer electrolytes for direct methanol fuel cell	Proton conductivity of 214×10^{-3} S/cm (58% improvement). Water sorption of 36.5 (90% improvement). The ion exchange capacity of 1.13 meq/g (24% improvement). Methanol crossover density of 89 mA/cm^2 (87% lower than pristine Nafion). Peak power density of 165 mW/cm^2 (154% improvement).	The addition of hydrophilic sulfonated h-BN enhanced the membrane water uptake and provided a better proton-conducting pathway. The presence of $-SO_3H$ groups in the functionalized h-BN also improved the ion exchange capacity barrier effect in h-BN due to hindering the methanol crossover.	[149]

Table 3. *Cont.*

Application	Platform	Role of 2D h-BN	Device Characteristics	Mechanisms	Ref.
Fuel cell	sPPO/h-BN	Reinforcement of the polymer electrolytes used in direct methanol fuel cell	Proton conductivity of 4.64×10^{-2} S/cm (67% improvement). Water sorption of 50.61% (55% improvement). The ion Ion exchange capacity of 1.92 meq/g (23% improvement). Methanol permeability of 2.04×10^{-7} cm^2/s (3 times lower than pristine sPPO). Peak power density of 122 mW/cm^2 (103% improvement).	π-π interactions between sBN and sPPO and introducing long-range proton-conducting pathways owing to the presence of excess sulfonic acid groups and hydrogen bonding bridge. The barrier effect of h-BN due to impermeability to methanol.	[153]
Fuel cell	SPEEK/PANI/h-BN	Reinforcement of the polymer electrolyte for direct methanol fuel cell	Proton conductivity of 4.13×10^{-3} S/cm (141% improvement). Water sorption of 58.42 (38% improvement). The ion Ion exchange capacity of 1.76 meq/g (9.4% improvement). Methanol permeability of 3.08×10^{-7} cm^2/s (46% lower than pristine SPEEK). Peak power density of 11.38 mW/cm^2 (23% improvement).	The surface defects in acidified h-BN surface formed new pathways for water molecules transport inside the SPEEK. The barrier effect in h-BN hindered the methanol crossover.	[154]
Fuel cell	rGO/h-BN/Fe_2O_3	The cathode catalyst of a microbial fuel cell	The maximum potential of 250 mVOpen circuit potential of 663 mV Power density of 1673 mW/m^2 (81% of the conventional Pt/C electrode)	Enhancement of the surface area for facile transport of reactants and electrons into r-GO.	[155]
Fuel cell	h-BN/glass	Compressive seal in a solid oxide fuel cell	Having leakage rates lower than 0.012 sccm/cm under input gas pressure of 6.8 kPa (better than the leakage rates of Al_2O_3-based compressive seals, 0.02 sccm/cm)	Gradual formation of liquid B_2O_3 films on the h-BN surface, improving bondage for both interface and interior particles.	[162]
Fuel cell	h-BN coating on ZrO_2 powders	Hydrogen environmental barrier coating	Effective against hydrogen diffusion up to 1713 K.	The high activation energy of 3.25 eV for atomic hydrogen diffusion into the (001) hexagonal BN surface.	[160]
Solar cell	p^+-InP/i-InP/h-BN/ITO	Passivation of p^+-InP/i-InP	FF of 75% (33% better than passivated device) Maximum efficiency of 17.2% (50% better than unpassivated device) The interface defect density of 2×10^{12} /eV cm^2	Surface passivation through the charge transfer from the surface defect states to 2D h-BN.	[170]
Solar cell	MoS_2/WSe_2/h-BN	Passivation of MoS_2/WSe_2	J_{SC} of 1.69 mA/cm^2 (37.5% improvement) and V_{OC} of 0.38 V (25.7% improvement) 74% improvement in PCE. Increase the average recombination lifetime from 112 ps to 131 ps before and after the addition of the h-BN layer. Long-term stability of the device.	Surface passivation through the charge transfer from the surface defect states to 2D h-BN.	[169]
Solar cell	TiO_2/h-BN/CdSe/P3HT	Surface passivation of mesoporous TiO_2	J_{SC} of 15.3 mA/cm^2 (40% improvement), and V_{OC} of 0.719 V (8.4% improvement). The maximum power output of 4.9×10^{-4} W (44% improvement), and PCE of 7% (46% improvement). Maximum EQE of 79% at 510 nm (23% improvement).	Surface passivation through the charge transfer from the surface defect states to 2D h-BN.	[182]

Table 3. *Cont.*

Application	Platform	Role of 2D h-BN	Device Characteristics	Mechanisms	Ref.
Solar cell	Dye-sensitized cell	Surface passivation of TiO_2	J_{SC} of 15.7 mA/cm^2 (23% improvement), and V_{OC} of 0.782 V (1.6% improvement). Maximum power of 5.72×10^{-4} W (57% improvement). PCE of 8.2% (58% improvement).	Minimizing electron-hole recombination at the TiO_2/dye/electrolyte interfaces.	[178]
Solar cell	Si /h-BN/graphene	The interface design of graphene/Si heterojunction	J_{SC} of 33.49 mA/cm^2 (28% improvement), and V_{OC} of 0.547 V (33% improvement). FF of 60.8% (75% improvement. The series resistance of 1.9 Ω (21% less than the system without h-BN). reverse saturation current density of 2.56×10^{-4} mA/cm^2 (one order of magnitude)	Appropriate band alignment and effective electron-blocking/hole-transporting mechanism	[173]
Solar cell	$AuCl_3$:MoS_2/h-BN/GaAs	The interface design of MoS_2/GaAs heterojunction	J_{SC} of 20.8 mA/cm^2 (1% improvement), and V_{OC} of 0.64 V (14% improvement). FF of 53.7% (15% improvement). PCE of 7.15% (33% improvement).Series resistance of 45.9 Ω (22% less than undoped system and without h-BN).	Appropriate band alignment and effective electron-blocking/hole-transporting mechanism	[180]
Solar cell	graphene/h-BN/GaAs	Interface design of graphene/GaAs heterojunction	Barrier height heterostructure of 1.02 eV (compare with 0.88 eV for the device without h-BN). PCE of 10.18% (18% improvement)	Appropriate band alignment and effective electron-blocking/hole-transporting mechanism	[181]
Solar cell	Si/h-BN interface	Interface of graphene/Si heterojunction	J_{SC} of 30 mA/cm2 (19% improvement), and V_{OC} of 0.42 V (2.4% improvement). FF of 71% (4.2% improvement). PCE of 8.94% (26.3% improvement).	Appropriate band alignment and effective electron-blocking/hole-transporting	[183]

3. Future Challenges and Remarks

To sum up, increasing 2D h-BN integration into energy production/storage units demonstrates the great intrinsic potential of this two-dimensional material for the energy industry. The electrical insulation of 2D h-BN allows the prevention of close contact between electrodes in a battery or where the separation of conductive parts is needed. The superior heat dissipation due to thermally conductive pathways of 2D h-BN provides much better control of heat management and safety concerns by minimizing heat accumulation. The partially ionic nature of bonds between boron and nitrogen in 2D h-BN lattice provides surface polarization and offers a prominent pathway for proton exchanges. Similarly, 2D h-BN can be incorporated into cathodic materials. The enhancement of electrolyte ionic conductivity, mechanical and thermal stability, and engineerability are other benefits of using 2D h-BN in energy research. The surface functionalization of 2D h-BN and its hybridization with other 2D materials have been effective for bandgap modulation.

Nevertheless, there are still challenges and gaps in our understanding of thickness-dependent characteristics of layered h-BN, charge transfer mechanisms on 2D h-BN surface via chemical reactions, electron tunneling through thin layers of h-BN, surface catalytic sites, and charge extraction mechanisms. Addressing these challenges could be a viable solution to enhance the applicability of 2D h-BN for energy applications. Generally, these challenges can be tackled by two different approaches: (1) integration of 2D h-BN into existing technologies and process optimization, (2) development of new products with h-BN as the core cell. In either case, the enhanced performance of the device is entangled with the surface chemical composition of 2D h-BN. From the formation of percolation networks in h-BN-based nanocomposites to enhancement of the lithium transference number of LIB, to

ionic conductivity and transparency for solar cell and proton exchange rates, they are all dependent on 2D h-BN surfaces characteristics. Simple and cost-effective synthesis methods, such as liquid exfoliation, often produce 2D h-BN with various functional groups/dopants. Therefore, regulating the synthesis condition leads to the enhancement of device efficiency. This becomes particularly important in thermoelectric applications where the negligible thermoelectric properties of 2D h-BN are considerably improved by functionalization of the basal plane, introducing point defects, modifying the edge chemistry, and hybridization with other 2D materials. In contrast, the need for bare 2D h-BN for voltaic cell applications may necessitate using more complex and costly approaches such as CVD.

The application of 2D h-BN in energy research is still at preliminary stages and besides batteries, supercapacitors, thermoelectrics, and fuel cells, other sustainable energy fields such as photovoltaics and solar cells are envisaged to benefit from the great separation characteristics of 2D h-BN.

Funding: This research was supported by Science Foundation Ireland (SFI) grant number 18/SIRG/5621 and Enterprise Ireland grant number CS20212089.

Conflicts of Interest: The authors declare no conflict of interest. The funders had no role in the design of the study; in the collection, analyses, or interpretation of data; in the writing of the manuscript, or in the decision to publish the results.

References

1. Gong, Y.; Xu, Z.-Q.; Li, D.; Zhang, J.; Aharonovich, I.; Zhang, Y. Two-Dimensional Hexagonal Boron Nitride for Building Next-Generation Energy-Efficient Devices. *ACS Energy Lett.* **2021**, *6*, 985–996. [CrossRef]
2. Zhang, D.; Zhang, S.; Yapici, N.; Oakley, R.; Sharma, S.; Parashar, V.; Yap, Y.K. Emerging Applications of Boron Nitride Nanotubes in Energy Harvesting, Electronics, and Biomedicine. *ACS Omega* **2021**, *6*, 20722–20728. [CrossRef]
3. Glavin, N.R.; Rao, R.; Varshney, V.; Bianco, E.; Apte, A.; Roy, A.; Ringe, E.; Ajayan, P.M. Emerging Applications of Elemental 2D Materials. *Adv. Mater.* **2020**, *32*, e1904302. [CrossRef]
4. Anasori, B.; Lukatskaya, M.R.; Gogotsi, Y. 2D metal carbides and nitrides (MXenes) for energy storage. *Nat. Rev. Mater.* **2017**, *2*, 16098. [CrossRef]
5. Angizi, S.; Akbar, M.A.; Darestani-Farahani, M.; Kruse, P. Review—Two-Dimensional Boron Carbon Nitride: A Comprehensive Review. *ECS J. Solid State Sci. Technol.* **2020**, *9*, 83004. [CrossRef]
6. Kaneti, Y.V.; Benu, D.P.; Xu, X.; Yuliarto, B.; Yamauchi, Y.; Golberg, D. Borophene: Two-dimensional Boron Monolayer: Synthesis, Properties, and Potential Applications. *Chem. Rev.* **2022**, *122*, 1000–1051. [CrossRef] [PubMed]
7. Angizi, S.; Alem, S.A.A.; Hasanzadeh Azar, M.; Shayeganfar, F.; Manning, M.I.; Hatamie, A.; Pakdel, A.; Simchi, A. A comprehensive review on planar boron nitride nanomaterials: From 2D nanosheets towards 0D quantum dots. *Prog. Mater. Sci.* **2022**, *124*, 100884. [CrossRef]
8. Han, R.; Liu, F.; Wang, X.; Huang, M.; Li, W.; Yamauchi, Y.; Sun, X.; Huang, Z. Functionalised hexagonal boron nitride for energy conversion and storage. *J. Mater. Chem. A* **2020**, *8*, 14384–14399. [CrossRef]
9. Khalaj, M.; Golkhatmi, S.Z.; Alem, S.A.A.; Baghchesaraee, K.; Azar, M.H.; Angizi, S. Recent Progress in the Study of Thermal Properties and Tribological Behaviors of Hexagonal Boron Nitride-Reinforced Composites. *J. Compos. Sci.* **2020**, *4*, 116. [CrossRef]
10. Pakdel, A.; Zhi, C.; Bando, Y.; Nakayama, T.; Golberg, D. Boron Nitride Nanosheet Coatings with Controllable Water Repellency. *ACS Nano* **2011**, *5*, 6507–6515. [CrossRef]
11. Zeng, H.; Zhi, C.; Zhang, Z.; Wei, X.; Wang, X.; Guo, W.; Bando, Y.; Golberg, D. "White Graphenes": Boron Nitride Nanoribbons via Boron Nitride Nanotube Unwrapping. *Nano Lett.* **2010**, *10*, 5049–5055. [CrossRef] [PubMed]
12. Pakdel, A.; Bando, Y.; Golberg, D. Plasma-Assisted Interface Engineering of Boron Nitride Nanostructure Films. *ACS Nano* **2014**, *8*, 10631–10639. [CrossRef] [PubMed]
13. Pakdel, A.; Bando, Y.; Golberg, D. Nano boron nitride flatland. *Chem. Soc. Rev.* **2014**, *43*, 934–959. [CrossRef]
14. Angizi, S.; Khalaj, M.; Alem, S.A.A.; Pakdel, A.; Willander, M.; Hatamie, A.; Simchi, A. Review—Towards the Two-Dimensional Hexagonal Boron Nitride (2D h-BN) Electrochemical Sensing Platforms. *J. Electrochem. Soc.* **2020**, *167*, 126513. [CrossRef]
15. Falin, A.; Cai, Q.; Santos, E.J.G.; Scullion, D.; Qian, D.; Zhang, R.; Yang, Z.; Huang, S.; Watanabe, K.; Taniguchi, T.; et al. Mechanical properties of atomically thin boron nitride and the role of interlayer interactions. *Nat. Commun.* **2017**, *8*, 15815. [CrossRef]
16. Angizi, S.; Yu, E.Y.C.; Dalmieda, J.; Saha, D.; Selvaganapathy, P.R.; Kruse, P. Defect Engineering of Graphene to Modulate pH Response of Graphene Devices. *Langmuir* **2021**, *37*, 12163–12178. [CrossRef] [PubMed]
17. Angizi, S.; Hatamie, A.; Ghanbari, H.; Simchi, A.A. Mechanochemical Green Synthesis of Exfoliated Edge-Functionalized Boron Nitride Quantum Dots: Application to Vitamin C Sensing through Hybridization with Gold Electrodes. *ACS Appl. Mater. Interfaces* **2018**, *10*, 28819–28827. [CrossRef]

18. Angizi, S.; Shayeganfar, F.; Azar, M.H.; Simchi, A. Surface/edge functionalized boron nitride quantum dots: Spectroscopic fingerprint of bandgap modification by chemical functionalization. *Ceram. Int.* **2020**, *46*, 978–985. [CrossRef]
19. Pakdel, A.; Zhi, C.; Bando, Y.; Golberg, D. Low-dimensional boron nitride nanomaterials. *Mater. Today* **2012**, *15*, 256–265. [CrossRef]
20. Lin, Y.; Williams, T.V.; Cao, W.; Elsayed-Ali, H.E.; Connell, J.W. Defect Functionalization of Hexagonal Boron Nitride Nanosheets. *J. Phys. Chem. C* **2010**, *114*, 17434–17439. [CrossRef]
21. Ma, P.; Spencer, J.T. Non-covalent stabilization and functionalization of boron nitride nanosheets (BNNSs) by organic polymers: Formation of complex BNNSs-containing structures. *J. Mater. Sci.* **2015**, *50*, 313–323. [CrossRef]
22. Weng, Q.; Wang, X.; Wang, X.; Bando, Y.; Golberg, D. Functionalized hexagonal boron nitride nanomaterials: Emerging properties and applications. *Chem. Soc. Rev.* **2016**, *45*, 3989–4012. [CrossRef] [PubMed]
23. Ren, J.; Stagi, L.; Innocenzi, P. Hydroxylated boron nitride materials: From structures to functional applications. *J. Mater. Sci.* **2021**, *56*, 4053–4079. [CrossRef]
24. Pakdel, A.; Bando, Y.; Shtansky, D.; Golberg, D. Nonwetting and optical properties of BN nanosheet films. *Surf. Innov.* **2013**, *1*, 32–39. [CrossRef]
25. Wang, X.; Pakdel, A.; Zhang, J.; Weng, Q.; Zhai, T.; Zhi, C.; Golberg, D.; Bando, Y. Large-surface-area BN nanosheets and their utilization in polymeric composites with improved thermal and dielectric properties. *Nanoscale Res. Lett.* **2012**, *7*, 662. [CrossRef]
26. Radhakrishnan, S.; Das, D.; Samanta, A.; de los Reyes, C.A.; Deng, L.; Alemany, L.B.; Weldeghiorghis, T.K.; Khabashesku, V.N.; Kochat, V.; Jin, Z.; et al. Fluorinated h-BN as a magnetic semiconductor. *Sci. Adv.* **2017**, *3*, e1700842. [CrossRef] [PubMed]
27. Li, X.; Wu, X.; Zeng, X.C.; Yang, J. Band-Gap Engineering via Tailored Line Defects in Boron-Nitride Nanoribbons, Sheets, and Nanotubes. *ACS Nano* **2012**, *6*, 4104–4112. [CrossRef] [PubMed]
28. Mballo, A.; Srivastava, A.; Sundaram, S.; Vuong, P.; Karrakchou, S.; Halfaya, Y.; Gautier, S.; Voss, P.L.; Ahaitouf, A.; Salvestrini, J.P.; et al. Towards P-Type Conduction in Hexagonal Boron Nitride: Doping Study and Electrical Measurements Analysis of hBN/AlGaN Heterojunctions. *Nanomaterials* **2021**, *11*, 211. [CrossRef]
29. Singh, R.S.; Tay, R.Y.; Chow, W.L.; Tsang, S.H.; Mallick, G.; Teo, H.T.E. Band gap effects of hexagonal boron nitride using oxygen plasma. *Appl. Phys. Lett.* **2014**, *104*, 163101. [CrossRef]
30. Herrera-Reinoza, N.; dos Santos, A.C.; de Lima, L.H.; Landers, R.; de Siervo, A. Atomically Precise Bottom-Up Synthesis of h-BNC: Graphene Doped with h-BN Nanoclusters. *Chem. Mater.* **2021**, *33*, 2871–2882. [CrossRef]
31. Emanet, M.; Şen, O.; Taşkin, I.; Çulha, M. Synthesis, Functionalization, and Bioapplications of Two-Dimensional Boron Nitride Nanomaterials. *Front. Bioeng. Biotechnol.* **2019**, *7*. [CrossRef]
32. Krečmarová, M.; Canet-Albiach, R.; Pashaei-Adl, H.; Gorji, S.; Muñoz-Matutano, G.; Nesládek, M.; Martínez-Pastor, J.P.; Sánchez-Royo, J.F. Extrinsic Effects on the Optical Properties of Surface Color Defects Generated in Hexagonal Boron Nitride Nanosheets. *ACS Appl. Mater. Interfaces* **2021**, *13*, 46105–46116. [CrossRef] [PubMed]
33. Uchida, Y.; Kawahara, K.; Fukamachi, S.; Ago, H. Chemical Vapor Deposition Growth of Uniform Multilayer Hexagonal Boron Nitride Driven by Structural Transformation of a Metal Thin Film. *ACS Appl. Electron. Mater.* **2020**, *2*, 3270–3278. [CrossRef]
34. Zhang, B.; Wu, Q.; Yu, H.; Bulin, C.; Sun, H.; Li, R.; Ge, X.; Xing, R. High-Efficient Liquid Exfoliation of Boron Nitride Nanosheets Using Aqueous Solution of Alkanolamine. *Nanoscale Res. Lett.* **2017**, *12*, 1–7. [CrossRef]
35. Zheng, X.; Wang, G.; Huang, F.; Liu, H.; Gong, C.; Wen, S.; Hu, Y.; Zheng, G.; Chen, D. Liquid Phase Exfoliated Hexagonal Boron Nitride/Graphene Heterostructure Based Electrode Toward Asymmetric Supercapacitor Application. *Front. Chem.* **2019**, *7*, 544. [CrossRef]
36. Kim, J.; Kwon, S.; Cho, D.-H.; Kang, B.; Kwon, H.; Kim, Y.; Park, S.O.; Jung, G.Y.; Shin, E.; Kim, W.-G.; et al. Direct exfoliation and dispersion of two-dimensional materials in pure water via temperature control. *Nat. Commun.* **2015**, *6*, 8294. [CrossRef]
37. Cao, L.; Emami, S.; Lafdi, K. Large-scale exfoliation of hexagonal boron nitride nanosheets in liquid phase. *Mater. Express* **2014**, *4*, 165–171. [CrossRef]
38. Deepika, D.; Li, L.H.; Glushenkov, A.M.; Hait, S.K.; Hodgson, P.; Chen, Y. High-Efficient Production of Boron Nitride Nanosheets via an Optimized Ball Milling Process for Lubrication in Oil. *Sci. Rep.* **2014**, *4*, 7288. [CrossRef] [PubMed]
39. Tian, Z.; Chen, K.; Sun, S.; Zhang, J.; Cui, W.; Xie, Z.; Liu, G. Crystalline boron nitride nanosheets by sonication-assisted hydrothermal exfoliation. *J. Adv. Ceram.* **2019**, *8*, 72–78. [CrossRef]
40. Liu, Q.; Hu, C.; Wang, X. One-pot solvothermal synthesis of water-soluble boron nitride nanosheets and fluorescent boron nitride quantum dots. *Mater. Lett.* **2018**, *234*, 306–310. [CrossRef]
41. Mahdizadeh, A.; Farhadi, S.; Zabardasti, A. Microwave-assisted rapid synthesis of graphene-analogue hexagonal boron nitride (h-BN) nanosheets and their application for the ultrafast and selective adsorption of cationic dyes from aqueous solutions. *RSC Adv.* **2017**, *7*, 53984–53995. [CrossRef]
42. Coleman, J.N.; Lotya, M.; O'Neill, A.; Bergin, S.D.; King, P.J.; Khan, U.; Young, K.; Gaucher, A.; De, S.; Smith, R.J.; et al. Two-Dimensional Nanosheets Produced by Liquid Exfoliation of Layered Materials. *Science* **2011**, *331*, 568–571. [CrossRef] [PubMed]
43. Bao, J.; Zhu, L.; Wang, H.; Han, S.; Jin, Y.; Zhao, G.; Zhu, Y.; Guo, X.; Hou, J.; Yin, H.; et al. Hexagonal Boron Nitride/Blue Phosphorene Heterostructure as a Promising Anode Material for Li/Na-Ion Batteries. *J. Phys. Chem. C* **2018**, *122*, 23329–23335. [CrossRef]

44. Shi, X.; Wang, K.; Tian, J.; Yin, X.; Guo, B.; Xi, G.; Wang, W.; Wu, W. Few-Layer Hydroxyl-Functionalized Boron Nitride Nanosheets for Nanoscale Thermal Management. *ACS Appl. Nano Mater.* **2020**, *3*, 2310–2321. [CrossRef]
45. Huang, K.; Liang, L.; Chai, S.; Tumuluri, U.; Li, M.; Wu, Z.; Sumpter, B.G.; Dai, S. Aminopolymer functionalization of boron nitride nanosheets for highly efficient capture of carbon dioxide. *J. Mater. Chem. A* **2017**, *5*, 16241–16248. [CrossRef]
46. Muhabie, A.A.; Cheng, C.-C.; Huang, J.-J.; Liao, Z.-S.; Huang, S.-Y.; Chiu, C.-W.; Lee, D.-J. Non-Covalently Functionalized Boron Nitride Mediated by a Highly Self-Assembled Supramolecular Polymer. *Chem. Mater.* **2017**, *29*, 8513–8520. [CrossRef]
47. Kong, D.; Zhang, D.; Guo, H.; Zhao, J.; Wang, Z.; Hu, H.; Xu, J.; Fu, C. Functionalized Boron Nitride Nanosheets/Poly(l-lactide) Nanocomposites and Their Crystallization Behavior. *Polymers* **2019**, *11*, 440. [CrossRef]
48. Li, Y.; Gao, D.; Zhao, S.; Xiao, Y.; Guo, Z.; Fang, Y.; Lin, J.; Liu, Z.; Huang, Y.; Guo, K.; et al. Carbon doped hexagonal boron nitride nanoribbon as efficient metal-free electrochemical nitrogen reduction catalyst. *Chem. Eng. J.* **2021**, *410*, 128419. [CrossRef]
49. Liu, Y.; Li, L.; Li, Q.; Lin, J.; Guo, Z.; Zhang, X.; Lu, Z.; Ma, Y.; Huang, Y.; Tang, C. Fluorine doped porous boron nitride for efficient CO2 capture and separation: A DFT study. *Appl. Surf. Sci.* **2021**, *556*, 149775. [CrossRef]
50. Lei, W.; Zhang, H.; Wu, Y.; Zhang, B.; Liu, D.; Qin, S.; Liu, Z.; Liu, L.; Ma, Y.; Chen, Y. Oxygen-doped boron nitride nanosheets with excellent performance in hydrogen storage. *Nano Energy* **2014**, *6*, 219–224. [CrossRef]
51. Chen, Y.; Xu, X.; Li, C.; Bendavid, A.; Westerhausen, M.T.; Bradac, C.; Toth, M.; Aharonovich, I.; Tran, T.T. Bottom-Up Synthesis of Hexagonal Boron Nitride Nanoparticles with Intensity-Stabilized Quantum Emitters. *Small* **2021**, *17*, 2008062. [CrossRef] [PubMed]
52. Kainthola, A.; Bijalwan, K.; Negi, S.; Sharma, H.; Dwivedi, C. Hydrothermal synthesis of highly stable boron nitride nanoparticles. *Mater. Today Proc.* **2020**, *28*, 138–140. [CrossRef]
53. Jing, X.; Puglisi, F.M.; Akinwande, D.; Lanza, M. Chemical vapor deposition of hexagonal boron nitride on metal-coated wafers and transfer-free fabrication of resistive switching devices. *2D Mater.* **2019**, *6*, 35021. [CrossRef]
54. McLean, B.D.; Webber, G.B.; Page, A.J. Boron Nitride Nucleation Mechanism during Chemical Vapor Deposition. *J. Phys. Chem. C* **2018**, *122*, 24341–24349. [CrossRef]
55. Ren, X.; Dong, J.; Yang, P.; Li, J.; Lu, G.; Wu, T.; Wang, H.; Guo, W.; Zhang, Z.; Ding, F.; et al. Grain boundaries in chemical-vapor-deposited atomically thin hexagonal boron nitride. *Phys. Rev. Mater.* **2019**, *3*, 14004. [CrossRef]
56. Han, D.; Zhang, J.; Weng, Z.; Kong, D.; Tao, Y.; Ding, F.; Ruan, D.; Yang, Q.-H. Two-dimensional materials for lithium/sodium-ion capacitors. *Mater. Today Energy* **2019**, *11*, 30–45. [CrossRef]
57. Chen, K.-S.; Balla, I.; Luu, N.S.; Hersam, M.C. Emerging Opportunities for Two-Dimensional Materials in Lithium-Ion Batteries. *ACS Energy Lett.* **2017**, *2*, 2026–2034. [CrossRef]
58. Rojaee, R.; Shahbazian-Yassar, R. Two-Dimensional Materials to Address the Lithium Battery Challenges. *ACS Nano* **2020**, *14*, 2628–2658. [CrossRef]
59. Peng, L.; Zhu, Y.; Chen, D.; Ruoff, R.S.; Yu, G. Two-Dimensional Materials for Beyond-Lithium-Ion Batteries. *Adv. Energy Mater.* **2016**, *6*, 1600025. [CrossRef]
60. Jeong, J.-M.; Choi, B.G.; Lee, S.C.; Lee, K.G.; Chang, S.-J.; Han, Y.-K.; Lee, Y.B.; Lee, H.U.; Kwon, S.; Lee, G.; et al. Hierarchical Hollow Spheres of Fe2O3@Polyaniline for Lithium Ion Battery Anodes. *Adv. Mater.* **2013**, *25*, 6250–6255. [CrossRef]
61. Li, X.; Lai, C.; Xiao, C.; Gao, X. Enhanced high rate capability of dual-phase Li4Ti5O12–TiO2 induced by pseudocapacitive effect. *Electrochim. Acta* **2011**, *56*, 9152–9158. [CrossRef]
62. Li, H.; Tay, R.Y.; Tsang, S.H.; Liu, W.; Teo, E.H.T. Reduced Graphene Oxide/Boron Nitride Composite Film as a Novel Binder-Free Anode for Lithium Ion Batteries with Enhanced Performances. *Electrochim. Acta* **2015**, *166*, 197–205. [CrossRef]
63. Zhang, F.; Németh, K.; Bareño, J.; Dogan, F.; Bloom, I.D.; Shaw, L.L. Experimental and theoretical investigations of functionalized boron nitride as electrode materials for Li-ion batteries. *RSC Adv.* **2016**, *6*, 27901–27914. [CrossRef]
64. Ma, T.; Wang, R.; Jin, S.; Zheng, S.; Li, L.; Shi, J.; Cai, Y.; Liang, J.; Tao, Z. Functionalized Boron Nitride-Based Modification Layer as Ion Regulator Toward Stable Lithium Anode at High Current Densities. *ACS Appl. Mater. Interfaces* **2021**, *13*, 391–399. [CrossRef]
65. de Moraes, A.C.M.; Hyun, W.J.; Seo, J.T.; Downing, J.R.; Lim, J.; Hersam, M.C. Ion-Conductive, Viscosity-Tunable Hexagonal Boron Nitride Nanosheet Inks. *Adv. Funct. Mater.* **2019**, *29*, 1902245. [CrossRef]
66. Rodrigues, M.-T.F.; Kalaga, K.; Gullapalli, H.; Babu, G.; Reddy, A.L.M.; Ajayan, P.M. Hexagonal Boron Nitride-Based Electrolyte Composite for Li-Ion Battery Operation from Room Temperature to 150 °C. *Adv. Energy Mater.* **2016**, *6*, 1600218. [CrossRef]
67. Waqas, M.; Ali, S.; Lv, W.; Chen, D.; Boateng, B.; He, W. High-Performance PE-BN/PVDF-HFP Bilayer Separator for Lithium-Ion Batteries. *Adv. Mater. Interfaces* **2019**, *6*, 1801330. [CrossRef]
68. De Moraes, A.C.M.; Hyun, W.J.; Luu, N.S.; Lim, J.-M.; Park, K.-Y.; Hersam, M.C. Phase-Inversion Polymer Composite Separators Based on Hexagonal Boron Nitride Nanosheets for High-Temperature Lithium-Ion Batteries. *ACS Appl. Mater. Interfaces* **2020**, *12*, 8107–8114. [CrossRef]
69. Orendorff, C.J.; Lambert, T.N.; Chavez, C.A.; Bencomo, M.; Fenton, K.R. Polyester Separators for Lithium-Ion Cells: Improving Thermal Stability and Abuse Tolerance. *Adv. Energy Mater.* **2013**, *3*, 314–320. [CrossRef]
70. Yu, L.; Miao, J.; Lin, J.Y.S.; Jin, Y. A comparative study on polypropylene separators coated with different inorganic materials for lithium-ion batteries. *Front. Chem. Sci. Eng.* **2017**, *11*, 346–352. [CrossRef]
71. Rahman, M.M.; Mateti, S.; Cai, Q.; Sultana, I.; Fan, Y.; Wang, X.; Hou, C.; Chen, Y. High temperature and high rate lithium-ion batteries with boron nitride nanotubes coated polypropylene separators. *Energy Storage Mater.* **2019**, *19*, 352–359. [CrossRef]

72. Le, H.T.T.; Ngo, D.T.; Kalubarme, R.S.; Cao, G.; Park, C.-N.; Park, C.-J. Composite Gel Polymer Electrolyte Based on Poly(vinylidene fluoride-hexafluoropropylene) (PVDF-HFP) with Modified Aluminum-Doped Lithium Lanthanum Titanate (A-LLTO) for High-Performance Lithium Rechargeable Batteries. *ACS Appl. Mater. Interfaces* **2016**, *8*, 20710–20719. [CrossRef]
73. Shim, J.; Kim, H.J.; Kim, B.G.; Kim, Y.S.; Kim, D.-G.; Lee, J.-C. 2D boron nitride nanoflakes as a multifunctional additive in gel polymer electrolytes for safe, long cycle life and high rate lithium metal batteries. *Energy Environ. Sci.* **2017**, *10*, 1911–1916. [CrossRef]
74. Monroe, C.; Newman, J. The Impact of Elastic Deformation on Deposition Kinetics at Lithium/Polymer Interfaces. *J. Electrochem. Soc.* **2005**, *152*, A396–A404. [CrossRef]
75. Varzi, A.; Raccichini, R.; Passerini, S.; Scrosati, B. Challenges and prospects of the role of solid electrolytes in the revitalization of lithium metal batteries. *J. Mater. Chem. A* **2016**, *4*, 17251–17259. [CrossRef]
76. Dukovic, J.O.; Tobias, C.W. Simulation of Leveling in Electrodeposition. *J. Electrochem. Soc.* **1990**, *137*, 3748–3755. [CrossRef]
77. Wu, J.; Li, X.; Rao, Z.; Xu, X.; Cheng, Z.; Liao, Y.; Yuan, L.; Xie, X.; Li, Z.; Huang, Y. Electrolyte with boron nitride nanosheets as leveling agent towards dendrite-free lithium metal anodes. *Nano Energy* **2020**, *72*, 104725. [CrossRef]
78. Ding, F.; Xu, W.; Graff, G.L.; Zhang, J.; Sushko, M.L.; Chen, X.; Shao, Y.; Engelhard, M.H.; Nie, Z.; Xiao, J.; et al. Dendrite-Free Lithium Deposition via Self-Healing Electrostatic Shield Mechanism. *J. Am. Chem. Soc.* **2013**, *135*, 4450–4456. [CrossRef] [PubMed]
79. Kim, D.; Liu, X.; Yu, B.; Mateti, S.; O'Dell, L.A.; Rong, Q.; Chen, Y. Amine-Functionalized Boron Nitride Nanosheets: A New Functional Additive for Robust, Flexible Ion Gel Electrolyte with High Lithium-Ion Transference Number. *Adv. Funct. Mater.* **2020**, *30*, 1910813. [CrossRef]
80. Aydın, H.; Çelik, S.; Bozkurt, A. Electrolyte loaded hexagonal boron nitride/polyacrylonitrile nanofibers for lithium ion battery application. *Solid State Ionics* **2017**, *309*, 71–76. [CrossRef]
81. Venkateswarlu, G.; Madhu, D.; Rani, J.V. Graphene Supported Boron Nitride Nanosheets as Advanced Electroanalytical Performance for Rechargeable Magnesium Storage System. *ChemistrySelect* **2020**, *5*, 2247–2254. [CrossRef]
82. Zhang, R.; Ling, C. Status and challenge of Mg battery cathode. *MRS Energy Sustain.* **2016**, *3*, 1. [CrossRef]
83. Venkateswarlu, G.; Madhu, D.; Rani, J.V. An effective performance of F-Doped hexagonal boron nitride nanosheets as cathode material in magnesium battery. *Mater. Chem. Phys.* **2019**, *226*, 356–361. [CrossRef]
84. Liang, Y.; Feng, R.; Yang, S.; Ma, H.; Liang, J.; Chen, J. Rechargeable Mg Batteries with Graphene-like MoS2 Cathode and Ultrasmall Mg Nanoparticle Anode. *Adv. Mater.* **2010**, *23*, 640–643. [CrossRef] [PubMed]
85. Xue, T.; Fan, H.J. From aqueous Zn-ion battery to Zn-MnO2 flow battery: A brief story. *J. Energy Chem.* **2021**, *54*, 194–201. [CrossRef]
86. Chen, D.; Kang, C.; Duan, W.; Yuan, Z.; Li, X. A non-ionic membrane with high performance for alkaline zinc-iron flow battery. *J. Membr. Sci.* **2020**, *618*, 118585. [CrossRef]
87. Lu, W.; Xu, P.; Shao, S.; Li, T.; Zhang, H.; Li, X. Multifunctional Carbon Felt Electrode with N-Rich Defects Enables a Long-Cycle Zinc-Bromine Flow Battery with Ultrahigh Power Density. *Adv. Funct. Mater.* **2021**, 2102913. [CrossRef]
88. Jian, Q.P.; Wu, M.C.; Jiang, H.R.; Lin, Y.K.; Zhao, T.S. A trifunctional electrolyte for high-performance zinc-iodine flow batteries. *J. Power Sources* **2020**, *484*, 229238. [CrossRef]
89. Hu, J.; Yue, M.; Zhang, H.; Yuan, Z.; Li, X. A Boron Nitride Nanosheets Composite Membrane for a Long-Life Zinc-Based Flow Battery. *Angew. Chem. Int. Ed.* **2020**, *59*, 6715–6719. [CrossRef]
90. Gong, K.; Xu, F.; Grunewald, J.B.; Ma, X.; Zhao, Y.; Gu, S.; Yan, Y. All-Soluble All-Iron Aqueous Redox-Flow Battery. *ACS Energy Lett.* **2016**, *1*, 89–93. [CrossRef]
91. Khor, A.; Leung, P.; Mohamed, M.R.; Flox, C.; Xu, Q.; An, L.; Wills, R.G.A.; Morante, J.R.; Shah, A.A. Review of zinc-based hybrid flow batteries: From fundamentals to applications. *Mater. Today Energy J.* **2018**, *8*, 80–108. [CrossRef]
92. Nejati, K.; Hosseinian, A.; Bekhradnia, A.; Vessally, E.; Edjlali, L. Na-ion batteries based on the inorganic BN nanocluster anodes: DFT studies. *J. Mol. Graph. Model.* **2017**, *74*, 1–7. [CrossRef]
93. Song, L.; Ci, L.; Lu, H.; Sorokin, P.B.; Jin, C.; Ni, J.; Kvashnin, A.G.; Kvashnin, D.G.; Lou, J.; Yakobson, B.I.; et al. Large Scale Growth and Characterization of Atomic Hexagonal Boron Nitride Layers. *Nano Lett.* **2010**, *10*, 3209–3215. [CrossRef]
94. Kansara, S.; Gupta, S.K.; Sonvane, Y.; Pajtler, M.V.; Ahuja, R. Inquisitive Geometric Sites in h-BN Monolayer for Alkali Earth Metal Ion Batteries. *J. Phys. Chem. C* **2019**, *123*, 19340–19346. [CrossRef]
95. Nejati, K.; Hosseinian, A.; Edjlali, L.; Vessally, E. The effect of structural curvature on the cell voltage of BN nanotube based Na-ion batteries. *J. Mol. Liq.* **2017**, *229*, 167–171. [CrossRef]
96. Ergen, O. Hexagonal boron nitride incorporation to achieve high performance Li4Ti5O12 electrodes. *AIP Adv.* **2020**, *10*, 45040. [CrossRef]
97. Wang, T.; Zhang, S.; Yin, L.; Li, C.; Xia, C.; An, Y.; Wei, S.Y. Silicene/boron nitride heterostructure for the design of highly efficient anode materials in lithium-ion battery. *J. Phys. Condens. Matter* **2020**, *32*, 355502. [CrossRef]
98. Fan, Y.; Liu, D.; Rahman, M.; Tao, T.; Lei, W.; Mateti, S.; Yu, B.; Wang, J.; Yang, C.; Chen, Y. Repelling Polysulfide Ions by Boron Nitride Nanosheet Coated Separators in Lithium–Sulfur Batteries. *ACS Appl. Energy Mater.* **2019**, *2*, 2620–2628. [CrossRef]
99. Chen, Y.; Kang, Q.; Jiang, P.; Huang, X. Rapid, high-efficient and scalable exfoliation of high-quality boron nitride nanosheets and their application in lithium-sulfur batteries. *Nano Res.* **2020**, *14*, 2424–2431. [CrossRef]

100. Hyun, W.J.; De Moraes, A.C.M.; Lim, J.-M.; Downing, J.R.; Park, K.-Y.; Tan, M.T.Z.; Hersam, M.C. High-Modulus Hexagonal Boron Nitride Nanoplatelet Gel Electrolytes for Solid-State Rechargeable Lithium-Ion Batteries. *ACS Nano* **2019**, *13*, 9664–9672. [CrossRef]
101. Qui, M.; Jia, H.; Lan, C.; Liu, H.; Fu, S. An enhanced kinetics and ultra-stable zinc electrode by functionalized boron nitride intermediate layer engineering. *Energy Storage Mater.* **2022**, *45*, 1175–1182. [CrossRef]
102. Gao, T.; Gong, L.-J.; Wang, Z.; Yang, Z.-K.; Pan, W.; He, L.; Zhang, J.; Ou, E.-C.; Xiong, Y.; Xu, W. Boron nitride/reduced graphene oxide nanocomposites as supercapacitors electrodes. *Mater. Lett.* **2015**, *159*, 54–57. [CrossRef]
103. Maity, C.K.; Goswami, N.; Verma, K.; Sahoo, S.; Nayak, G.C. A facile synthesis of boron nitride supported zinc cobalt sulfide nano hybrid as high-performance pseudocapacitive electrode material for asymmetric supercapacitors. *J. Energy Storage* **2020**, *32*, 101993. [CrossRef]
104. Saha, S.; Jana, M.; Samanta, P.; Murmu, N.C.; Kim, N.H.; Kuila, T.; Lee, J.H. Investigation of band structure and electrochemical properties of h-BN/rGO composites for asymmetric supercapacitor applications. *Mater. Chem. Phys.* **2017**, *190*, 153–165. [CrossRef]
105. Maity, C.K.; Santra, D.K.; Verma, K.; Sahoo, S.; Cotts, S.; Akinwande, D.; Berry, V.; Nayak, G.C. Induced conducting energy-levels in a boron nitride nano-framework for asymmetric supercapacitors in high charge-mobility ionic electrolytes. *Compos. Part B Eng.* **2021**, *212*, 108728. [CrossRef]
106. Rajendran, J.; Reshetilov, A.N.; Sundramoorthy, A.K. Preparation of hybrid paper electrode based on hexagonal boron nitride integrated graphene nanocomposite for free-standing flexible supercapacitors. *RSC Adv.* **2021**, *11*, 3445–3451. [CrossRef]
107. Maity, C.K.; Sahoo, S.; Verma, K.; Behera, A.K.; Nayak, G.C. Facile functionalization of boron nitride (BN) for the development of high-performance asymmetric supercapacitors. *New J. Chem.* **2020**, *44*, 8106–8119. [CrossRef]
108. Gunday, S.T.; Cevik, E.; Yusuf, A.; Bozkurt, A. Nanocomposites composed of sulfonated polysulfone/hexagonal boron nitride/ionic liquid for supercapacitor applications. *J. Energy Storage* **2019**, *21*, 672–679. [CrossRef]
109. Stoller, M.D.; Park, S.; Zhu, Y.; An, J.; Ruoff, R.S. Graphene-Based Ultracapacitors. *Nano Lett.* **2008**, *8*, 3498–3502. [CrossRef]
110. Wang, C.; Hu, K.; Liu, Y.; Zhang, M.-R.; Wang, Z.; Li, Z. Flexible Supercapacitors Based on Graphene/Boron Nitride Nanosheets Electrodes and PVA/PEI Gel Electrolytes. *Materials* **2021**, *14*, 1955. [CrossRef]
111. Li, T.; Jiao, X.; You, T.; Dai, F.; Zhang, P.; Yu, F.; Hu, L.; Ding, L.; Zhang, L.; Wen, Z.; et al. Hexagonal boron nitride nanosheet/carbon nanocomposite as a high-performance cathode material towards aqueous asymmetric supercapacitors. *Ceram. Int.* **2019**, *45*, 4283–4289. [CrossRef]
112. Song, F.; Chen, Q.; Li, Y.; Li, Y.; Zhang, L. High energy density supercapacitors based on porous mSiO2@Ni3S2/NiS2 promoted with boron nitride and carbon. *Chem. Eng. J.* **2020**, *390*, 124561. [CrossRef]
113. Byun, S.; Kim, J.H.; Song, S.H.; Lee, M.; Park, J.-J.; Lee, G.; Hong, S.H.; Lee, D. Ordered, Scalable Heterostructure Comprising Boron Nitride and Graphene for High-Performance Flexible Supercapacitors. *Chem. Mater.* **2016**, *28*, 7750–7756. [CrossRef]
114. Hassan, M.; Gondal, M.A.; Cevik, E.; Qahtan, T.F.; Bozkurt, A.; Dastageer, M.A. High performance pliable supercapacitor fabricated using activated carbon nanospheres intercalated into boron nitride nanoplates by pulsed laser ablation technique. *Arab. J. Chem.* **2020**, *13*, 6696–6707. [CrossRef]
115. Saha, S.; Jana, M.; Khanra, P.; Samanta, P.; Koo, H.; Murmu, N.C.; Kuila, T. Band Gap Engineering of Boron Nitride by Graphene and Its Application as Positive Electrode Material in Asymmetric Supercapacitor Device. *ACS Appl. Mater. Interfaces* **2015**, *7*, 14211–14222. [CrossRef]
116. Khan, A.F.; Down, M.P.; Smith, G.C.; Foster, C.W.; Banks, C.E. Surfactant-exfoliated 2D hexagonal boron nitride (2D-hBN): Role of surfactant upon the electrochemical reduction of oxygen and capacitance applications. *J. Mater. Chem. A* **2017**, *5*, 4103–4113. [CrossRef]
117. Hu, J.; Xie, K.; Liu, X.; Guo, S.; Shen, C.; Liu, X.; Li, X.; Wang, J.-G.; Wei, B. Dramatically Enhanced Ion Conductivity of Gel Polymer Electrolyte for Supercapacitor via h-BN Nanosheets Doping. *Electrochim. Acta* **2017**, *227*, 455–461. [CrossRef]
118. Zheng, S.; Lei, W.; Qin, J.; Wu, Z.-S.; Zhou, F.; Wang, S.; Shi, X.; Sun, C.; Chen, Y.; Bao, X. All-solid-state high-energy planar asymmetric supercapacitors based on all-in-one monolithic film using boron nitride nanosheets as separator. *Energy Storage Mater.* **2018**, *10*, 24–31. [CrossRef]
119. Mohammed, M.H. Electronic and thermoelectric properties of zigzag and armchair boron nitride nanotubes in the presence of C island. *Chin. J. Phys.* **2018**, *56*, 1622–1632. [CrossRef]
120. Pakdel, A.; Guo, Q.; Nicolosi, V.; Mori, T. Enhanced thermoelectric performance of Bi–Sb–Te/Sb2O3 nanocomposites by energy filtering effect. *J. Mater. Chem. A* **2018**, *6*, 21341–21349. [CrossRef]
121. Vishkayi, S.I.; Tagani, M.B.; Soleimani, H.R. Enhancement of thermoelectric efficiency by embedding hexagonal boron-nitride cells in zigzag graphene nanoribbons. *J. Phys. D Appl. Phys.* **2015**, *48*. [CrossRef]
122. Khan, A.U.; Orabi, R.A.R.A.; Pakdel, A.; Vaney, J.-B.; Fontaine, B.; Gautier, R.; Halet, J.-F.; Mitani, S.; Mori, T. Sb Doping of Metallic CuCr2S4 as a Route to Highly Improved Thermoelectric Properties. *Chem. Mater.* **2017**, *29*, 2988–2996. [CrossRef]
123. Pan, C.; Long, M.; He, J. Enhanced thermoelectric properties in boron nitride quantum-dot. *Results Phys.* **2017**, *7*, 1487–1491. [CrossRef]
124. Mir, S.H. A computational study of physical, electronic, thermal and transport properties of one-dimensional boron and boron nitride systems. *J. Solid State Chem.* **2021**, *297*, 122037. [CrossRef]

125. Jiang, X.; Ban, C.; Li, L.; Wang, C.; Chen, W.; Liu, X. Thermoelectric properties study on the BN nanoribbons via BoltzTrap first-principles. *AIP Adv.* **2021**, *11*, 55120. [CrossRef]
126. Zberecki, K.; Swirkowicz, R.; Barnaś, J. Boron nitride zigzag nanoribbons: Optimal thermoelectric systems. *Phys. Chem. Chem. Phys.* **2015**, *17*, 22448–22454. [CrossRef] [PubMed]
127. Kanahashi, K.; Pu, J.; Takenobu, T. 2D Materials for Large-Area Flexible Thermoelectric Devices. *Adv. Energy Mater.* **2020**, *10*, 1902842. [CrossRef]
128. Xie, Z.-X.; Tang, L.-M.; Pan, C.-N.; Chen, Q.; Chen, K.-Q. Ballistic thermoelectric properties in boron nitride nanoribbons. *J. Appl. Phys.* **2013**, *114*, 144311. [CrossRef]
129. Tran, V.-T.; Saint-Martin, J.; Dollfus, P. High thermoelectric performance in graphene nanoribbons by graphene/BN interface engineering. *Nanotechnology* **2015**, *26*, 495202. [CrossRef]
130. Wang, J.; Mu, X.; Wang, X.; Wang, N.; Ma, F.; Liang, W.; Sun, M. The thermal and thermoelectric properties of in-plane C-BN hybrid structures and graphene/h-BN van der Waals heterostructures. *Mater. Today Phys.* **2018**, *5*, 29–57. [CrossRef]
131. Wu, J.; Liu, Y.; Liu, Y.; Cai, Y.; Zhao, Y.; Ng, H.K.; Watanabe, K.; Taniguchi, T.; Zhang, G.; Qiu, C.W.; et al. Large enhancement of thermoelectric performance in MoS2/h-BN heterostructure due to vacancy-induced band hybridization *Proc. Natl. Acad. Sci. USA* **2020**, *117*, 18127. [CrossRef]
132. Ma, T.; Lin, C.-T.; Wang, Y. The dimensionality effect on phonon localization in graphene/hexagonal boron nitride superlattices. *2D Mater.* **2020**, *7*, 35029. [CrossRef]
133. Chen, C.-C.; Li, Z.; Shi, L.; Cronin, S.B. Thermoelectric transport across graphene/hexagonal boron nitride/graphene heterostructures. *Nano Res.* **2014**, *8*, 666–672. [CrossRef]
134. Li, X.; Yin, J.; Zhou, J.; Wang, Q.; Guo, W. Exceptional high Seebeck coefficient and gas-flow-induced voltage in multilayer graphene. *Appl. Phys. Lett.* **2012**, *100*, 183108. [CrossRef]
135. Cho, S.; Kang, S.D.; Kim, W.; Lee, E.-S.; Woo, S.-J.; Kong, K.-J.; Kim, I.; Kim, H.-D.; Zhang, T.; Stroscio, J.A.; et al. Thermoelectric imaging of structural disorder in epitaxial graphene. *Nat. Mater.* **2013**, *12*, 913–918. [CrossRef] [PubMed]
136. Mahan, G.D.; Sofo, J.O.; Bartkowiak, M. Multilayer thermionic refrigerator and generator. *J. Appl. Phys.* **1998**, *83*, 4683–4689. [CrossRef]
137. D'Souza, R.; Mukherjee, S. Thermoelectric transport in graphene/h-BN/graphene heterostructures: A computational study. *Phys. E Low-Dimens. Syst. Nanostructures* **2016**, *81*, 96–101. [CrossRef]
138. Nakamura, J.; Akaishi, A. Anomalous enhancement of Seebeck coefficients of the graphene/hexagonal boron nitride composites. *Jpn. J. Appl. Phys.* **2016**, *55*, 1102A9. [CrossRef]
139. Yang, K.; Chen, Y.; D'Agosta, R.; Xie, Y.; Zhong, J.; Rubio, A. Enhanced thermoelectric properties in hybrid graphene/boron nitride nanoribbons. *Phys. Rev. B* **2012**, *86*, 1–8. [CrossRef]
140. Algharagholy, L.; Al-Galiby, Q.; Marhoon, H.A.; Sadeghi, H.; Abduljalil, H.M.; Lambert, C.J. Tuning thermoelectric properties of graphene/boron nitride heterostructures. *Nanotechnology* **2015**, *26*, 475401. [CrossRef]
141. Duan, S.; Cui, Y.; Yi, W.; Chen, X.; Yang, B.; Liu, X. Superior Conversion Efficiency Achieved in GeP3/h-BN Heterostructures as Novel Flexible and Ultralight Thermoelectrics. *ACS Appl. Mater. Interfaces* **2021**, *13*, 18800–18808. [CrossRef] [PubMed]
142. Gouda, M.H.; Tamer, T.; Konsowa, A.H.; Farag, H.; Eldin, M.M. Organic-Inorganic Novel Green Cation Exchange Membranes for Direct Methanol Fuel Cells. *Energies* **2021**, *14*, 4686. [CrossRef]
143. Velayutham, P.; Sahu, A.K.; Parthasarathy, S. A Nafion-Ceria Composite Membrane Electrolyte for Reduced Methanol Crossover in Direct Methanol Fuel Cells. *Energies* **2017**, *10*, 259. [CrossRef]
144. Falcão, D.S.; Silva, R.A.; Rangel, C.M.; Pinto, A.M.F.R. Performance of an Active Micro Direct Methanol Fuel Cell Using Reduced Catalyst Loading MEAs. *Energies* **2017**, *10*, 1683. [CrossRef]
145. Braz, B.A.; Oliveira, V.B.; Pinto, A.M.F.R. Experimental Evaluation of the Effect of the Anode Diffusion Layer Properties on the Performance of a Passive Direct Methanol Fuel Cell. *Energies* **2020**, *13*, 5198. [CrossRef]
146. Zhou, Z.; Zholobko, O.; Wu, X.-F.; Aulich, T.; Thakare, J.; Hurley, J. Polybenzimidazole-Based Polymer Electrolyte Membranes for High-Temperature Fuel Cells: Current Status and Prospects. *Energies* **2021**, *14*, 135. [CrossRef]
147. Song, H.-B.; Park, J.-H.; Park, J.-S.; Kang, M.-S. Pore-Filled Proton-Exchange Membranes with Fluorinated Moiety for Fuel Cell Application. *Energies* **2021**, *14*, 4433. [CrossRef]
148. Kregar, A.; Frühwirt, P.; Ritzberger, D.; Jakubek, S.; Katrašnik, T.; Gescheidt, G. Sensitivity Based Order Reduction of a Chemical Membrane Degradation Model for Low-Temperature Proton Exchange Membrane Fuel Cells. *Energies* **2020**, *13*, 5611. [CrossRef]
149. Parthiban, V.; Sahu, A.K. Performance enhancement of direct methanol fuel cells using a methanol barrier boron nitride–Nafion hybrid membrane. *New J. Chem.* **2020**, *44*, 7338–7349. [CrossRef]
150. Yan, X.; Sun, J.; Gao, L.; Zheng, W.; Dai, Y.; Ruan, X.; He, G. A novel long-side-chain sulfonated poly(2,6-dimethyl-1,4-phenylene oxide) membrane for vanadium redox flow battery. *Int. J. Hydrogen Energy* **2018**, *43*, 301–310. [CrossRef]
151. Guan, R.; Gong, C.; Lu, D.; Zou, H.; Lu, W. Development and characterization of homogeneous membranes prepared from sulfonated poly(phenylene oxide). *J. Appl. Polym. Sci.* **2005**, *98*, 1244–1250. [CrossRef]
152. Shaari, N.; Kamarudin, S.K. Recent advances in additive-enhanced polymer electrolyte membrane properties in fuel cell applications: An overview. *Int. J. Energy Res.* **2019**, *43*, 2756–2794. [CrossRef]

153. Yadav, V.; Niluroutu, N.; Bhat, S.D.; Kulshrestha, V. Insight toward the Electrochemical Properties of Sulfonated Poly(2,6-dimethyl-1,4-phenylene oxide) via Impregnating Functionalized Boron Nitride: Alternate Composite Polymer Electrolyte for Direct Methanol Fuel Cell. *ACS Appl. Energy Mater.* **2020**, *3*, 7091–7102. [CrossRef]
154. Yogarathinam, L.T.; Jaafar, J.; Ismail, A.F.; Goh, P.S.; Gangasalam, A.; Hanifah, M.F.R.; Wong, K.C.; Subramaniam, M.N.; Peter, J. Functionalized boron nitride embedded sulfonated poly (ether ether ketone) proton exchange membrane for direct methanol fuel cell applications. *J. Environ. Chem. Eng.* **2021**, *9*, 105876. [CrossRef]
155. Mahalingam, S.; Ayyaru, S.; Ahn, Y.-H. Enhanced cathode performance of Fe2O3, boron nitride-doped rGO nanosheets for microbial fuel cell applications. *Sustain. Energy Fuels* **2020**, *4*, 1454–1468. [CrossRef]
156. Mahato, N.; Banerjee, A.; Gupta, A.; Omar, S.; Balani, K. Progress in material selection for solid oxide fuel cell technology: A review. *Prog. Mater. Sci.* **2015**, *72*, 141–337. [CrossRef]
157. Checchetto, R.; Chayahara, A.; Horino, H.; Miotello, A.; Fujii, K. A study of deuterium permeation through thin BN films. *Thin Solid Films* **1997**, *299*, 5–9. [CrossRef]
158. Checchetto, R.; Miotello, A. Deuterium diffusion through hexagonal boron nitride thin films. *J. Appl. Phys.* **2000**, *87*, 110–116. [CrossRef]
159. He, L.; Wang, H.; Chen, L.; Wang, X.; Xie, H.; Jiang, C.; Lingxiu, C.; Elibol, K.; Meyer, J.; Watanabe, K.; et al. Isolating hydrogen in hexagonal boron nitride bubbles by a plasma treatment. *Nat. Commun.* **2019**, *10*, 1–9. [CrossRef] [PubMed]
160. Bull, S.K.; Champ, T.A.; Raj, S.V.; O'Brien, R.C.; Musgrave, C.B.; Weimer, A.W. Atomic Layer Deposited Boron Nitride Nanoscale Films Act as High Temperature Hydrogen Barriers. *Appl. Surf. Sci.* **2021**, *565*, 150428. [CrossRef]
161. Weimer, A.W. Particle atomic layer deposition. *J. Nanoparticle Res.* **2019**, *21*, 1–42. [CrossRef] [PubMed]
162. Li, R.; Wang, X.; Peng, L.; Jiang, B.; Yang, J.; Yan, D.; Pu, J.; Chi, B.; Li, J. Thermal cycling stability of novel hexagonal boron nitride (h-BN)/glass compressive seals for planar intermediate temperature solid oxide fuel cells. *J. Alloys Compd.* **2020**, *843*, 155620. [CrossRef]
163. Kim, J.-H.; Kim, D.-H.; So, J.-H.; Koo, H.-J. Toward Eco-Friendly Dye-Sensitized Solar Cells (DSSCs): Natural Dyes and Aqueous Electrolytes. *Energies* **2021**, *15*, 219. [CrossRef]
164. Cao, V.M.H.; Bae, J.; Shim, J.; Hong, B.; Jee, H.; Lee, J. Fabrication of the Cu_2ZnSnS_4 Thin Film Solar Cell via a Photo-Sintering Technique. *Appl. Sci.* **2021**, *12*, 38. [CrossRef]
165. Alhamada, T.F.; Hanim, M.A.A.; Jung, D.W.; Nuraini, A.A.; Hasan, W.Z.W. A Brief Review of the Role of 2D Mxene Nanosheets toward Solar Cells Efficiency Improvement. *Nanomaterials* **2021**, *11*, 2732. [CrossRef]
166. Kalita, G.; Kobayashi, M.; Shaarin, M.D.; Mahyavanshi, R.D.; Tanemura, M. Schottky Barrier Diode Characteristics of Graphene-GaN Heterojunction with Hexagonal Boron Nitride Interfacial Layer. *Phys. Status Solidi* **2018**, *215*, 1800089. [CrossRef]
167. Xu, S.J.; Luo, Y.F.; Zhong, W.; Xiao, Z.H.; Liu, X.Y. Investigation of Hexagonal Boron Nitride for Application as Counter Electrode in Dye-Sensitized Solar Cells. *Adv. Mater. Res.* **2012**, *512*, 242–245. [CrossRef]
168. Lee, G.-H.; Cuong, T.-V.; Yeo, D.-K.; Cho, H.; Ryu, B.-D.; Kim, E.-M.; Nam, T.-S.; Suh, E.-K.; Seo, T.-H.; Hong, C.-H. Hexagonal Boron Nitride Passivation Layer for Improving the Performance and Reliability of InGaN/GaN Light-Emitting Diodes. *Appl. Sci.* **2021**, *11*, 9321. [CrossRef]
169. Cho, A.-J.; Kwon, J.-Y. Hexagonal Boron Nitride for Surface Passivation of Two-Dimensional van der Waals Heterojunction Solar Cells. *ACS Appl. Mater. Interfaces* **2019**, *11*, 39765–39771. [CrossRef]
170. Raj, V.; Chugh, D.; Black, L.E.; Shehata, M.M.; Li, L.; Kremer, F.; Macdonald, D.H.; Tan, H.H.; Jagadish, C. Passivation of InP solar cells using large area hexagonal-BN layers. *NPJ 2D Mater. Appl.* **2021**, *5*, 1–8. [CrossRef]
171. Lee, W.-C.; Hu, C. Modeling gate and substrate currents due to conduction- and valence-band electron and hole tunneling [CMOS technology]. In *Proceedings of the 2000 Symposium on VLSI Technology, Honolulu, HI, USA, 15 –17 June 2000*; Digest of Technical Papers; IEEE: Piscataway, NJ, USA, 2002. [CrossRef]
172. Rienacker, M.; Bossmeyer, M.; Merkle, A.; Romer, U.; Haase, F.; Krugener, J.; Brendel, R.; Peibst, R. Notice of Removal Junction resistivity of carrier selective polysilicon on oxide junctions and its impact on the solar cell performance. In Proceedings of the 2017 IEEE 44th Photovoltaic Specialist Conference (PVSC), Washington, DC, USA, 25–30 June 2017; Institute of Electrical and Electronics Engineers (IEEE): Piscataway, NJ, USA, 2018; pp. 1–7.
173. Meng, J.-H.; Liu, X.; Zhang, X.-W.; Zhang, Y.; Wang, H.-L.; Yin, Z.-G.; Zhang, Y.-Z.; Liu, H.; You, J.-B.; Yan, H. Interface engineering for highly efficient graphene-on-silicon Schottky junction solar cells by introducing a hexagonal boron nitride interlayer. *Nano Energy* **2016**, *28*, 44–50. [CrossRef]
174. Arifin, Z.; Suyitno, S.; Hadi, S.; Sutanto, B. Improved Performance of Dye-Sensitized Solar Cells with TiO2 Nanoparticles/Zn-Doped TiO2 Hollow Fiber Photoanodes. *Energies* **2018**, *11*, 2922. [CrossRef]
175. Nien, Y.-H.; Chen, H.-H.C.; Hsu, H.-H.; Rangasamy, M.; Hu, G.-M.; Yong, Z.-R.; Kuo, P.-Y.; Chou, J.-C.; Lai, C.-H.; Ko, C.-C.; et al. Study of How Photoelectrodes Modified by TiO 2 / Ag Nanofibers in Various Structures Enhance the Low Illumination. *Energies* **2020**, *13*, 2248. [CrossRef]
176. Liu, L.; Wang, H.; Wang, D.; Li, Y.; He, X.; Zhang, H.; Shen, J. ZnO@TiO2 Core/Shell Nanowire Arrays with Different Thickness of TiO2 Shell for Dye-Sensitized Solar Cells. *Crystals* **2020**, *10*, 325. [CrossRef]
177. Tehare, K.K.; Navale, S.T.; Stadler, F.J.; He, Z.; Yang, H.; Xiong, X.; Liu, X.; Mane, R.S. Enhanced DSSCs performance of TiO_2 nanostructure by surface passivation layers. *Mater. Res. Bull.* **2018**, *99*, 491–495. [CrossRef]

178. Shanmugam, M.; Jacobs-Gedrim, R.; Durcan, C.; Yu, B. 2D layered insulator hexagonal boron nitride enabled surface passivation in dye sensitized solar cells. *Nanoscale* **2013**, *5*, 11275–11282. [CrossRef]
179. Tsuboi, Y.; Wang, F.; Kozawa, D.; Funahashi, K.; Mouri, S.; Miyauchi, Y.; Takenobu, T.; Matsuda, K. Enhanced photovoltaic performances of graphene/Si solar cells by insertion of a MoS2thin film. *Nanoscale* **2015**, *7*, 14476–14482. [CrossRef]
180. Lin, S.; Li, X.; Wang, P.; Xu, Z.; Zhang, S.; Zhong, H.; Wu, Z.; Xu, W.; Chen, H. Interface designed MoS2/GaAs heterostructure solar cell with sandwich stacked hexagonal boron nitride. *Sci. Rep.* **2015**, *5*, 15103. [CrossRef]
181. Li, X.; Lin, S.; Lin, X.; Xu, Z.; Wang, P.; Zhang, S.; Zhong, H.; Xu, W.; Wu, Z.; Fang, W. Graphene/h-BN/GaAs sandwich diode as solar cell and photodetector. *Opt. Express* **2016**, *24*, 134–145. [CrossRef]
182. Shanmugam, M.; Jain, N.; Jacobs-Gedrim, R.; Xu, Y.; Yu, B. Layered insulator hexagonal boron nitride for surface passivation in quantum dot solar cell. *Appl. Phys. Lett.* **2013**, *103*, 243904. [CrossRef]
183. Jabeen, M.; Haxha, S. 2D/3D graphene on h-BN interlayer-silicon solar cell with ZnO:Al buffer layer and enormous light captivation using Au/Ag NPs. *Opt. Express* **2020**, *28*, 12709–12728. [CrossRef] [PubMed]